Neogene Uplift and Magmatism of Anatolia: Insights from Drainage Analysis and Basaltic Geochemistry

F. McNab[1], P. W. Ball[1], M. J. Hoggard[1] and N. J. White[1]

[1]Bullard Laboratories, Department of Earth Sciences, University of Cambridge, Madingley Rise, Madingley Road, Cambridge, CB3 0EZ, UK.

Key Points:

- Regional uplift of East Anatolian Plateau intiates at ~20 Ma and propagates westward
- Elevated mantle potential temperatures decrease from east to west
- Neogene uplift and magmatism generated by asthenospheric thermal anomalies

Corresponding author: Fergus McNab, fm430@cam.ac.uk

Corresponding author: Nicky White, njw10@cam.ac.uk

Abstract

It is generally agreed that mantle dynamics have played a significant role in generating and maintaining the elevated topography of Anatolia during Neogene times. However, there is much debate about the relative importance of subduction zone and asthenospheric processes. Key issues concern onset and cause of regional uplift, thickness of the lithospheric plate, and the presence or absence of temperature and/or compositional anomalies within the convecting mantle. Here, we tackle these interlinked issues by analyzing and modeling two disparate suites of observations. First, a drainage inventory of 1,844 longitudinal river profiles is assembled. This geomorphic database is inverted to calculate the variation of Neogene regional uplift through time and space by minimizing the misfit between observed and calculated river profiles subject to independent calibration. Our results suggest that regional uplift commenced in the east at 20 Ma and propagated westward. Secondly, we have assembled a database of geochemical analyses of basaltic rocks. Two different approaches have been used to quantitatively model this database with a view to determining the depth and degree of asthenospheric melting across Anatolia. Our results suggest that melting occurs at depths as shallow as 60 km in the presence of mantle potential temperatures as high as 1400°C. There is evidence that potential temperatures are higher in the east, consistent with the pattern of sub-plate shear wave velocity anomalies. Our combined results are consistent with isostatic and admittance analyses and suggest that elevated asthenospheric temperatures beneath thinned Anatolian lithosphere have played a first order role in generating and maintaining regional dynamic topography and basaltic magmatism.

1 Introduction

The origin of Anatolian topography is the subject of considerable debate [*Şengör et al.*, 2003; *Göğüş and Psyklywec*, 2008; *Bartol and Govers*, 2014; *Schildgen et al.*, 2014]. The landscape is dominated by the low relief Central and East Anatolian Plateux, which have elevations of 1–2 km (Figure 1a; Table 1). A patchy distribution of marine sedimentary rocks indicates that large portions of eastern and Central Anatolia were below mean sea level until Middle and Late Miocene times, respectively [Figure 1b; *Poisson et al.*, 1996; *Hüsing et al.*, 2009; *Cosentino et al.*, 2012; *Schildgen et al.*, 2012a,b; *Cipollari et al.*, 2012, 2013; *Bartol and Govers*, 2014; *Schildgen et al.*, 2014]. Nevertheless, the spatial and temporal evolution of this topographic signature and the nature of the processes that drive regional uplift are not well understood.

Anatolia has undergone a complex tectonic history. During the Cenozoic era, gradual closure of the Neotethys Ocean was accommodated by subduction of oceanic lithosphere and by accretion of different crustal fragments, culminating in the collision of Arabia with Eurasia between Late Eocene and Early Miocene times [e.g. *Şengör and Yilmaz*, 1981; *Şengör et al.*, 2008; *Jolivet and Brun*, 2010; *van Hinsbergen et al.*, 2010; *Ballato et al.*, 2011; *McQuarrie and Van Hinsbergen*, 2013; *Schildgen et al.*, 2014].

Global positioning system (GPS) measurements of crustal displacements, earthquake focal mechanisms, and the distribution of active faults confirm that north-south shortening continues in Eastern Anatolia [Figure 1c; *Reilinger et al.*, 2006; *Şengör et al.*, 2008; *Nocquet*, 2012]. Since Miocene times, east-west translation and extension have dominated in Central and Western Anatolia [e.g. *McKenzie*, 1978; *Jackson and McKenzie*, 1988; *Aktuğ et al.*, 2009; *Aktuğ et al.*, 2013; *Isik et al.*, 2014; *Yıldırım et al.*, 2016]. It has been proposed that this westward motion is a manifestation of material extrusion caused by a combination of Arabia-Eurasia collision and roll-back of the Hellenic trench [*Şengör et al.*, 1985; *Le Pichon and Kreemer*, 2010]. Tractions on the base of the lithosphere imposed by flow of the sub-plate mantle and gradients in gravitational potential energy are invoked to drive these motions [*Faccenna et al.*, 2013, 2014; *England et al.*, 2016]. While crustal and lithospheric shortening probably played a role in causing regional uplift of the East Anato-

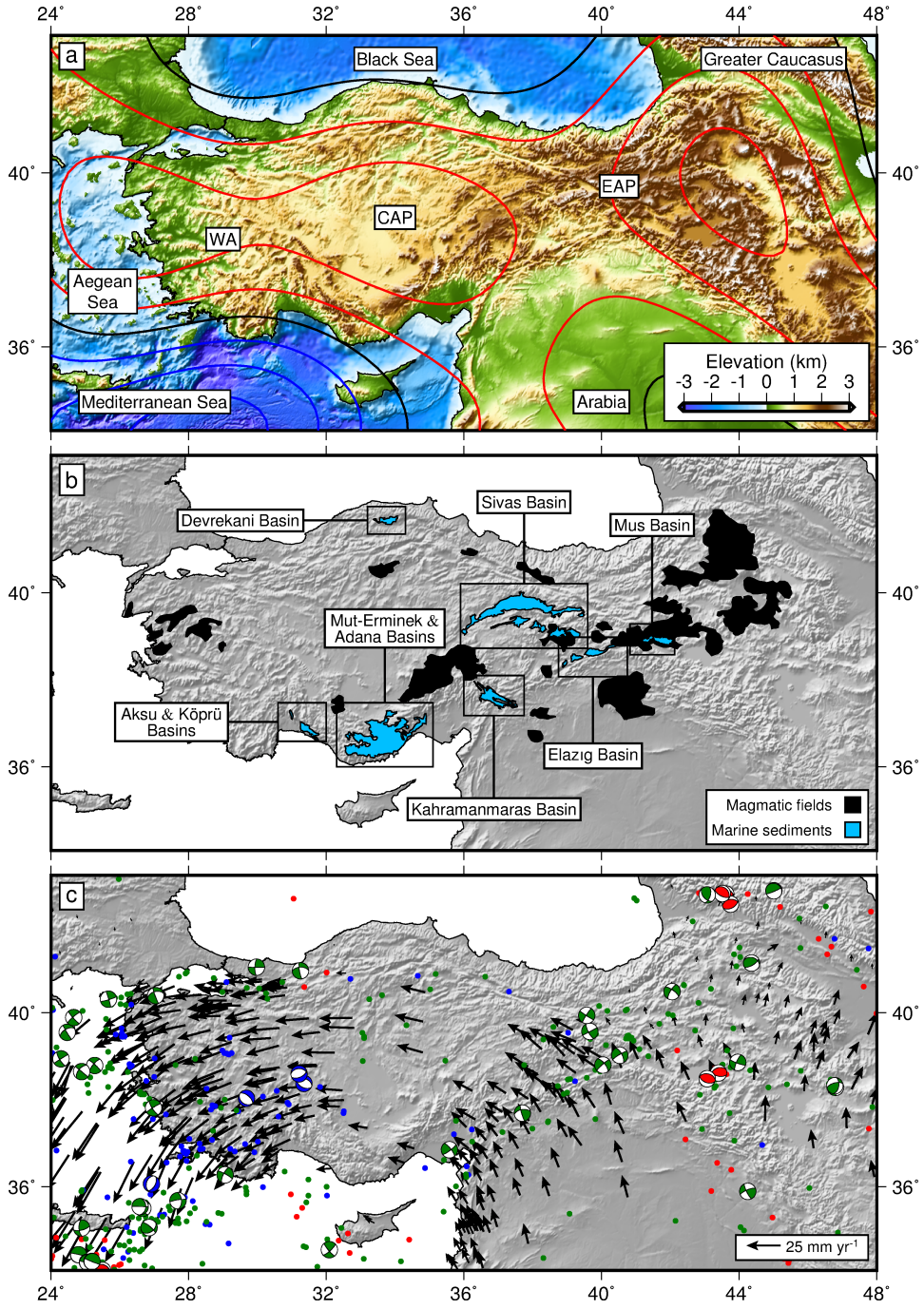

Figure 1. Tectonic setting of Anatolia. (a) Topographic map showing major geographic features. Red/black/blue contours = positive/zero/negative GGM03C free-air gravity anomalies filtered for wavelengths of 730–13,000 km and contoured at 25 mGal intervals; WA = Western Anatolia [*Tapley et al.*, 2007]; CAP = Central Anatolian Plateau; EAP = Eastern Anatolian Plateau. (b) Blue labeled polygons = Miocene marine sedimentary rocks [*Poisson et al.*, 1996; *Hüsing et al.*, 2009; *Cosentino et al.*, 2012; *Schildgen et al.*, 2012a,b; *Cipollari et al.*, 2012, 2013; *Bartol and Govers*, 2014; *Schildgen et al.*, 2014]; black polygons = Neogene basaltic volcanism [*Schildgen et al.*, 2014]. (c) Black arrows = deformation vectors with reference to Eurasian plate determined from GPS measurements [*Nocquet*, 2012]; colored beach balls = focal mechanisms of large earthquakes (M_W >6) taken from Centroid Moment Tensor Catalogue [*Dziewonski et al.*, 1981; *Ekström et al.*, 2012] where red = reverse, blue = normal and green = strike-slip events; small colored circles = smaller earthquakes (M_W <6).

55

Table 1. Marine sedimentary rocks of Anatolia.

Basin	Location	Marine Microfossil Fauna	Epoch (Stage)	Age (Ma)	Elevation (km)	Ref.
Mut-Ermenek	Sarıkavak	PF: *Globigerinoides tenellus*. C: *Calcidiscus macintyrei*; *Geophyocapsa caribbeanica* and *G. oceanica* (medium *G.*).	Pleistocene (Calabrian)	1.73–1.66	0.6–0.65	a, b
	Hacıahmetli	C: *Calcidiscus leptoporus*, small *Geophyocapsa*.	Pleistocene (Calabrian)	1.66–1.62	1.2	a, b
	Başyala	PF: *Orbulina suturalis* and *O. universa*; *Cataspidrax parvalus*; *Globigerinoides trilobus*, *G. quadrilobatus* and *G. extremus*. C: *Helicosphaera stalis* Theodorisis and *H. walbersdorfensis* T.; *Umbilicospaera jafari*	Miocene (Tortonian)	8.35–7.81	1.9	c, d
	Olukpınar	C: *Calcidiscus floridanus*; *Reticulofenestra pseudoumbicilus*; *Helicosphaera walbersdorfensis* and *H. carteri*; *Cocolithus pelagicus*.	Miocene (Serravallian)	13–12.5	1.65	d
Köprü	Sarıalan	PF: *Heterostegina* spp.; *Globigerinoides extremus*; *Sphaeroidinellopsis* spp.; *Orbulina universa*; *Globorotalia menardi*; *Siphonia reticulata*. BF: *Elphidium* spp.; *Lobatula lobatula*	Miocene (Tortonian)	7.17–6.7	1.5	e
Aksu	Gebiz	PF: *Globigerinoides trilobus*, *G. extremus*, *G. sacculifer* and *G. conglobatus*; *Globoturborotalia nepenthes*; *Globoratalia margaritae margaritae*, *G. m. evoluta* and *G. primitiva*. C: *Amaurolithus delicatus*; *Cyclococcolithus macintyrei*; *Discoaster brouweri*, *D. pentradiatus* and *D. surculus*; *Triquetrorhabdus rugosus*.	Pliocene (Zanclean)	5.3–3.6	0.45	f
Adana	Avadan	PF: *Sphaeroidinellopsis seminulia* and *S. disjuncta*; *Orbulina universa*; *Globigerinoides* spp. BF: *Lenticula* spp.; *Cibicides* spp. C: *Reticulofenstral zanclea* and *R. pseudoumbicilus*; *Helicosphaera carteri* and *H. intermedia*.	Pliocene (Zanclean)	5.3–5.2	0.35–0.65*	g
	Borehole T-191	PF: *Neogloboquadrina dutertrei* and *N. pachyderma*. BF: *Ammonia* spp.; *Elphidium* spp.	Pleistocene (Gelasian–Calabrian)	2.6–0.8	0.03–0.23*	g
Sivas	Central-Eastern Sivas	BF: *Miogypsinoides*; *Miogypsina*; *Nephrolepidina*. PF: *Globigerinoides trilobus*.	Miocene (Aquitian–Burgidalian)	23.0–16.0	1.5	h, i
Muş	Eastern Muş	PF: *Paragloborotalia pseudokugleri*, *P. siakensis*; *Globigerinoides primordius*.	Oligocene (Chattian)	25.9–23.0	1.5	j
Elazığ	Gevla	PF: *Paragloborotalia opima nana*; *Globigerina ciperoensis* and *G. angulisuturalis*; *Globigerinoides primordius*.	Oligocene (Chattian)	27.5–23.0	1.1	j
Kahramanmaraş	'Road', Avcılar	PF: *Globoratalia partimlabiata*; *Paragloborotalia siakensis*; *Globigerinoides subquadratus*. C: *Cyclicargolithus abisectus*; *Spenolithus heteromorphus*.	Miocene (Serravallian–Tortian)	12.8–9.9	0.8	j
Devrakani	—	BF: *Nummulites*; *Discocyclina*.	(Early) Miocene	23–16	1.1	k

* Total uplift including estimated water depths during deposition.
PF = planktic foraminifera, BF = benthic foraminifera, C = calcareous nannoplankton.
[a] *Yıldız et al.* [2003].
[b] *Schildgen et al.* [2012a].
[c] *Cosentino et al.* [2012]. Age consistent with ostracod assemblages and paleomagnetic analyses.
[d] *Cipollari et al.* [2013]. Echinoid, coral, bryzoa, sponge spicule bioclasts. Bioturbation (*Thalassinoides* and *Chondrites*).
[e] *Schildgen et al.* [2012b]. Patch coral reefs, sponge spicules, bryozoa, pebbles with *Lithofaga* borings. Age consistent with U-Pb zircon dating of reworked ash.
[f] *Poisson et al.* [2011]. Patch coral reefs, stromatolites. Age consistent with Ostracod assemblages.
[g] *Cipollari et al.* [2012]. Ages consistent with Ostracod assemblages.
[h] *Poisson et al.* [1996]. Patch and larger coral reefs. Sand bodies with gutter casts, hummocky cross stratification, 3D ripples; interpreted as storm deposits.
[i] *Çiner et al.* [2002].
[j] *Hüsing et al.* [2009]. Echinoderms, corals, sponges. Fining upward sand bodies with flute casts, displaced nummulites and gastropods; interpreted as turbiditic.
[k] *Tunoğlu* [1991, 1994].

lian Plateau, it is less easy to account for Late Neogene uplift of Western, and particularly Central Anatolia.

Plateau morphology and an apparent lack of crustal and lithospheric shortening have led many authors to invoke different lithospheric and asthenospheric processes in order to produce regional uplift. Examples include: steepening, tearing and breaking off of subducting African lithosphere; delamination of Anatolian lithosphere; lithospheric dripping; and upwelling asthenospheric thermal anomalies [*Şengör et al.*, 2003; *Göğüş and Psyklywec*, 2008; *Faccenna et al.*, 2013; *Bartol and Govers*, 2014; *Schildgen et al.*, 2014; *Göğüş et al.*, 2017]. Each of these mechanisms invokes arrival of asthenospheric mantle at shallow depths, where it provides isostatic and/or viscous topographic support. Positive long wavelength free-air gravity anomalies, slow *P*- and *S*-wave anomalies, together with elevated regional heatflow are all consistent with the presence of buoyant material within the uppermost mantle beneath Anatolia [*Biryol et al.*, 2011; *Bakırcı et al.*, 2012; *Salaün et al.*, 2012; *Chamorro et al.*, 2014; *Skolbeltsyn et al.*, 2014; *Govers and Fichtner*, 2016].

Coeval with this phase of Neogene regional uplift, basaltic magmatism has occurred throughout Anatolia [Figure 1b; *Keskin*, 2003; *Çoban*, 2007]. Geochemistry of these volcanic rocks should reflect processes involved in their generation. The most obvious feature is a clear shift from calc-alkaline (i.e. subduction related) to intra-plate alkaline magmatism during Miocene times. This shift is particularly well defined within Western Anatolia, although similar patterns have also been described in Central and Eastern Anatolia [*Wilson et al.*, 1997; *Innocenti et al.*, 2005; *Agostini et al.*, 2007; *Keskin*, 2007]. It is widely recognized that this shift reflects a change in melt-generating processes that may be linked to growth of regional uplift.

Here, we combine quantitative analysis of three different sets of observations to show how Neogene uplift and magmatism of Anatolia are related to ongoing processes within the asthenospheric mantle immediately beneath the lithospheric plate. First, we compile published receiver function estimates of crustal thickness to identify residual topographic anomalies. We also investigate the relationship between topography and free-air gravity anomalies to calculate the degree of flexural rigidity and to isolate long wavelength dynamic support of the Anatolian Plateaux. Secondly, we extract and model an inventory of longitudinal river profiles. This drainage inventory is inverted subject to independent geologic constraints to extract a regional uplift history. Finally, we compile whole-rock geochemical analyses for Neogene basaltic rocks. A combined forward and inverse modeling strategy is used to determine the depth and degree of melting. In this way, we investigate processes that potentially link magmatism, regional uplift, and the geodynamic evolution of Anatolia.

2 Crustal and Lithospheric Templates

2.1 Receiver Function Analyses

Several lines of evidence suggest that Neogene uplift of the Anatolian plateaux is not generated by crustal thickening alone [*Schildgen et al.*, 2014]. A significant consideration is the relationship between present-day elevation and crustal thickness. Here, we have assembled a database of crustal thickness estimates derived from published receiver function analyses (see Data Set S1 and references therein; Figure 2). These analyses use the recorded travel times and amplitudes of direct and converted phases from teleseismic earthquakes to constrain the shear wave velocity structure of the crust and upper mantle. Crustal thicknesses estimated in this way increase from $\sim$ 20 km in Western Anatolia to $\sim$ 50 km on the East Anatolian Plateau (Figure 2a). This pattern broadly reflects the way in which present-day crustal deformation changes from northeast-southwest extension in the west to north-south shortening in the east. In general, thicker crust has greater elevation.

It is instructive to compare the observed relationship between crustal thickness and elevation with that predicted by isostatic calculations. Recent studies attempt to determine the residual topography of Anatolia (i.e. that component of topographic elevation which is not accounted for by the observed thickness and density of the crust and lithospheric mantle; *Boschi et al.*, 2010; *Faccenna et al.*, 2013, 2014; *Uluocak et al.*, 2016). These studies exploit different data sources and reference frames such that estimates of residual topography vary between −2 and +2 km. Here, we balance idealized columns of continental lithosphere with different thicknesses and densities against the density structure of a mid-ocean ridge.

The elevation of a column of continental lithosphere, e, for a crustal thickness of t_{cc} is given by

$$e = t_{cc}\left(\frac{\rho_a - \rho_{cc}}{\rho_a}\right) - t_{oc}\left(\frac{\rho_a - \rho_{oc}}{\rho_a}\right) - s_w\left(\frac{\rho_a - \rho_w}{\rho_a}\right) + (a - t_{cc})\left(\frac{\rho_a - \rho_m}{\rho_a}\right), \quad (1)$$

where t_{oc} and ρ_{oc} are the thickness and density of oceanic crust, s_w and ρ_w are the thickness and density of water, and a is the lithospheric thickness (Figure 2). The average density of Anatolian crust, ρ_{cc} = 2.8 Mg m^{-3}, according to the EPcrust reference model [*Molinari and Morelli*, 2011]. Densities of asthenospheric mantle, ρ_a, and lithospheric mantle, ρ_m, are calculated by assuming an adiabatic temperature gradient and by including the effects of compressibility and putative chemical depletion (for detailed description see Supporting Information).

Here, we investigate two conceivable end members for the thermal structure of continental lithosphere. In the first case, the lithosphere is assumed to be thermally equilibrated (Figure 2b). The calculated elevation as a function of crustal thickness is shown in Figure 2d. In the second case, we simulate the loss or thinning of lithospheric material (e.g. delamination) without any heating of the remaining lithosphere toward a steady-state geothermal gradient (Figure 2e). In this disequilibrated case, continental lithosphere is colder and denser than equilibrated lithosphere of the same thickness, and so the expected elevation is lowered (Figure 2f and 2g).

In order to determine the degree to which changes in crustal thickness can account for observed elevation, lithospheric thickness must be estimated. Inevitably, these estimates are subject to considerable uncertainty. *Reid et al.* [2017] estimate lithospheric thicknesses of ∼ 60 km beneath Central Anatolia based on analysis of basaltic geochemistry. Estimates based upon receiver function analyses range between 60 and 90 km [*Çakır and Erduran*, 2011; *Angus et al.*, 2015; *Kind et al.*, 2015]. A reasonable upper bound for present-day lithospheric thickness is ∼ 120 km since a greater thickness would manifest itself as a substantial lithospheric root that should be visible in surface wave tomographic models [*Priestley and McKenzie*, 2013]. For this upper bound, present-day Anatolian topography is approximately in isostatic equilibrium. If lithospheric thickness is less than 90 km, Anatolia should have a residual topography of −1 km (i.e. it will be depressed with respect to the mid-oceanic ridge). Note that if the lithosphere beneath Anatolia is thermally disequilibrated following rapid loss of the lithosphere, a thinner lithosphere is required to achieve isostatic equilibrium. We emphasise that a significant source of uncertainty in these isostatic calculations is the density of the lithospheric mantle which can be reduced through depletion (i.e. become more hartzburgitic) by up to 60 kg m^{-3} [*Crosby et al.*, 2010]. Figure 2d and f show the effects that varying the density of lithospheric mantle upon elevation for different lithospheric thicknesses. Progressively depleted lithospheric mantle tends to increase expected elevations and hence lowers residual topographic estimates.

Scattered outcrops of emergent marine sedimentary rocks suggest that Anatolian Plateaux underwent 1–2 km of regional uplift during Neogene times. Isostatic relationships can provide useful quantitative insights into plausible mechanisms for this youthful regional uplift. First, regional uplift could be generated by a change in crustal thickness of

6–13 km (i.e. 15–33% crustal thickening; Figure 2d,g). However, present-day GPS velocities, earthquake focal mechanisms, and the planform of mapped Neogene faults suggest that this mechanism is unlikely, particularly for Central Anatolia [*McKenzie*, 1978; *Jackson and McKenzie*, 1988; *Şengör et al.*, 2008; *Aktuğ et al.*, 2009; *Nocquet*, 2012; *Aktuğ et al.*, 2013; *Isik et al.*, 2014; *Yıldırım et al.*, 2016]. Note that if crustal thickening were to occur by magmatic underplating, even larger thicknesses would be required because of the greater density of underplated material. Secondly, thinning of the lithospheric mantle has been proposed [*Şengör et al.*, 2003; *Göğüş and Psyklywec*, 2008; *Faccenna et al.*, 2013; *Bartol and Govers*, 2014; *Schildgen et al.*, 2014; *Göğüş et al.*, 2017]. Isostatic relationships suggest that removal of 75–125 km of undepleted lithospheric mantle could generate the required topographic response. This proposal requires Miocene lithospheric thicknesses of 150–200 km (Figure 2). Thirdly, a change in sub-plate support could have occurred (e.g. slab detachment and/or emplacement of anomolously hot asthenospheric material). Since the present-day relationship between crustal thickness and elevation suggests that Anatolia is approximately in isostatic equilibrium or slightly drawn down, this third mechanism requires Anatolia to have been convectively drawn down by a further 1–2 km during pre-Miocene times. We note in passing that oceanic lithosphere of the Black Sea to the north and of the East Mediterranean Sea to the south have negative residual depth anomalies of 1–2 km [*Hoggard et al.*, 2016, 2017].

2.2 Admittance Analysis

Anatolia has significant long wavelength free-air gravity anomalies of up to +50 mGal and so it is unlikely that its topography is maintained by crustal thickness and density variations alone (Figure 3b). In order to investigate the degree of support provided by flexural isostasy and by sub-plate density variation, the spectral relationship between topographic and gravity fields is analyzed (Figure 3).

Admittance, $Z(k)$, is the ratio between topography and coherent free-air gravity anomalies as a function of wavenumber, $k = 2\pi/\lambda$. Here, observed values of Z are calculated from the SRTM30_PLUS topography and EIGEN-6C gravity fields within a 650 $\times$ 1,500 km box using a two-dimensional multi-taper method [*Becker et al.*, 2009; *Förste et al.*, 2012; *McKenzie and Fairhead*, 1997]. At short (i.e. $<$ 150 km) wavelengths, Z is $\sim$ 100 mGal km^{-1} and at long (i.e. $>$ 300 km) wavelengths, Z is 30 $\pm$ 4 mGal km^{-1} (Figure 3c). Between 150 and 300 km, Z gradually decreases. Significantly, the degree of coherence between topography and gravity is greater than 0.5 which suggests that the observed variation of Z is robust (Figure 3e).

The rapid decrease in Z at intermediate wavelengths can be used to estimate the elastic thickness, T_e. Theoretical estimates of admittance are calculated for a suite of values of T_e using an idealized two-layer crustal model overlying a mantle half-space. The upper and lower crust are assigned thicknesses of 10 km and 25 km, and densities of 2.4 Mg m^{-3} and 2.9 Mg m^{-3}, respectively. T_e together with the fraction of internal loading that correlates with surface topography, F_2, are co-varied until a satisfactory fit between observed and calculated admittance is obtained [*McKenzie*, 2003]. A parameter sweep through $T_e - F_2$ space reveals a well-defined global minimum at T_e = 10.4 km and F_2 = 29%. This value is consistent with values of $T_e < 20$ km obtained from both free-air admittance and Bouguer coherency studies which used wavelet transforms [*Audet*, 2014].

The value of T_e controls the maximum wavelength over which loads can be supported by flexural isostasy. The half-wavelength of flexural support, x_b, for a line load imposed upon an unbroken plate is given by

$$x_b = \left[\frac{4\pi^4 E T_e^3}{12g(1-\sigma^2)(\rho_m - \rho_s)} \right]^{\frac{1}{4}}, \tag{2}$$

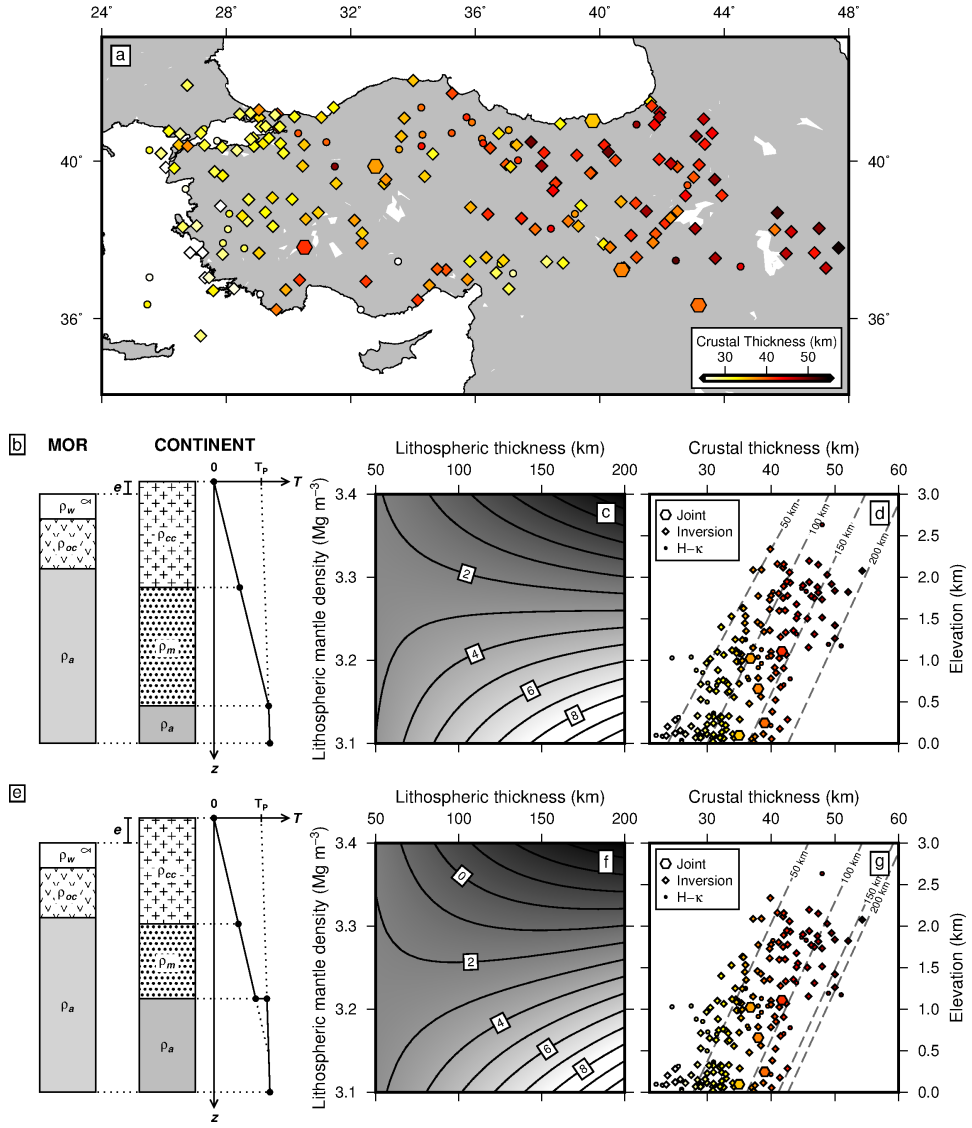

Figure 2. Crustal thickness estimates. (a) Map showing locations of published receiver function analyses colored according to crustal thickness. Circles = crustal thicknesses determined by H-κ stacking; diamonds = crustal thicknesses determined by inverse modeling; hexagons = crustal thicknesses determined by joint inverse modeling of receiver functions and surface wave dispersion observations. (b) Pair of cartoons showing oceanic and continental columns together with continental geothermal gradient used for Airy isostatic calculation if continental lithosphere is thermal equilibrated. (c) Calculated elevation plotted as function of lithospheric thickness and lithospheric mantle density for a crustal thickness of 40 km. Numbered boxes = elevation in kilometers. (d) Observed crustal thicknesses plotted as function of low-pass filtered (i.e. wavelengths>30 km) elevations. Dashed lines = crustal thickness as function of elevation for the equilibrated continental lithospheric thicknesses of 50–200 km. (e)-(g) Same for thermally disequilibrated continental lithosphere, following instantaneous thinning of 200 km lithosphere.

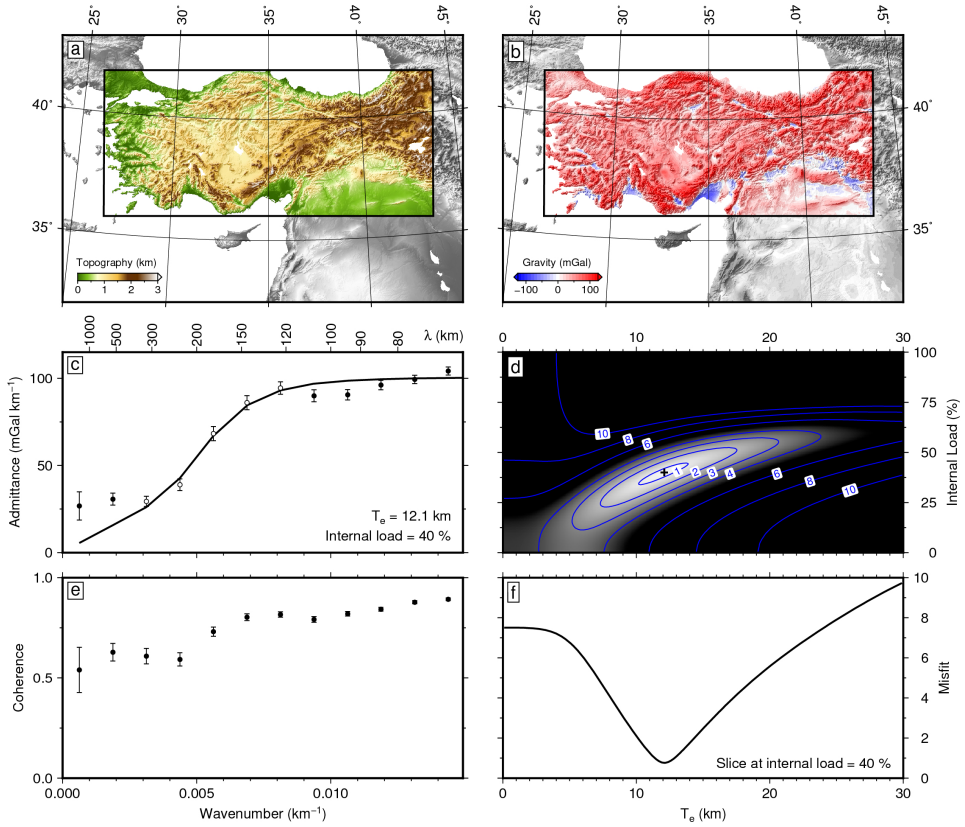

Figure 3. Admittance analysis of Anatolia. (a) SRTM30_PLUS topography [*Becker et al.*, 2009]. Box = 650×1500 km window of analysis. (b) EIGEN-6C free-air gravity anomalies [*Förste et al.*, 2012]. (c) Admittance for component of gravity anomalies that are coherent with topography plotted as function of wavenumber. Circles with vertical bars = observed admittance values $\pm 1\sigma$; black line = best-fitting elastic model with T_e = 10.4 km and F_2 = 29%; upper/lower crustal thicknesses and densities are 10/25 km and 2.4/2.9 Mg m^{-3}, respectively; at wavelength of 1000 km, Z = 30 ± 4 mGal km^{-1}. (d) Contoured misfit to open circles plotted as function of T_e and F_2. Black cross = locus of global minimum. (e) Coherence between gravity and topography as function of wavenumber. (f) Vertical slice through global minimum at F_2 = 40%. Doubling value of minimum misfit yields uncertainty range of $T_e = 10.4^{+1.7}{-1.5}$ km.

where $E = 70$ GPa is Young's modulus, $g = 9.81$ m s^{-2} is gravitational acceleration, $\sigma = 0.25$ is Poisson's ratio, $\rho_m = 3.3$ Mg m^{-3} is the density of the mantle, and ρ_s is the density of infilling material [*Gunn*, 1943]. For air-loaded topography, $T_e = 10.4^{+1.7}_{-1.5}$ km yields $x_b = 96^{+13}_{-11}$ km. This value is significantly smaller than the typical wavelengths of Anatolian plateaux, which suggests that flexural loading is unlikely to be the primary cause of this elevated interior.

A flexural isostatic model provides an excellent fit to observed admittance at wavelengths shorter than $\sim$ 300 km (Figure 3c). At longer wavelengths, Z does not tend to zero but instead approaches $+30\pm4$ mGal km^{-1}. Positive values of long-wavelength admittance are consistent with calculations of dynamic support for convection within the upper mantle [*McKenzie*, 2010; *Colli et al.*, 2016]. Negative long wavelength gravity anomalies occur immediately to the north of Anatolia in the Black Sea and to the south in the East Mediterranean Sea. These anomalies are consistent with negative residual depth measurements of 1–2 km that imply dynamic topographic drawdown [*Hoggard et al.*, 2016, 2017].

3 Inverse Modeling of River Profiles

3.1 Anatolian Drainage Networks

Emergent marine sedimentary rocks represent tangible evidence that specific locations throughout Anatolia have been uplifted in Neogene times. Nevertheless, the spatial and temporal pattern of regional epeirogeny remains poorly constrained [*Bartol and Govers*, 2014]. It is now recognized that fluvial landscapes are influenced in significant ways by regional tectonic forcing. An important corollary is that suites of longitudinal river profiles should indirectly record the regional uplift history [*Whipple*, 2009]. When landscapes are in equilibrium, these profiles tend to become concave upward. When uplift exceeds erosion, convex-upward shapes develop that give rise to long-wavelength knickzones. It has been shown that these observations can be exploited quantitatively by jointly inverting substantial inventories of profiles to calculate the spatial and temporal pattern of regional uplift rate [*Pritchard et al.*, 2009; *Roberts and White*, 2010; *Fox et al.*, 2014; *Goren et al.*, 2014; *Rudge et al.*, 2015]. We apply this inverse modeling approach to an Anatolian drainage network.

We first extracted a drainage network containing 1,844 rivers that covers most of Anatolia (Figure 4). A SRTM digital elevation model was decimated to yield a horizontal resolution of 170 m [*Becker et al.*, 2009]. Anomalous spikes and holes were removed and filled. Flow-routing algorithms were then used to recover a suite of river profiles and their associated upstream drainage areas as a function of distance [Data Set S2; *Tarboton*, 1997]. The fidelity of recovered river profiles was checked and verified using Landsat imagery. Putative river profiles that deviated significantly from actual profiles were excised. We also removed endorheic portions of drainage networks in the vicinity of Lakes Van, Tuz and Burdur.

Extracted river profiles from four major catchments that drain the Anatolian Plateaux are presented in Figure 5. The shapes of these profiles deviate significantly from equilibrated profiles which typically have concave-upward shapes. Significant knickpoints (i.e. short wavelength changes in slope) are primarily caused by intrinsic processes (e.g. lithologic contrasts, active faulting, artificial dams). However, profiles from these catchments also exhibit broad convex-upward knickzones with wavelengths of hundreds of kilometers and amplitudes of hundreds of meters. These knickzones tend to correlate within and between catchments. The northern edge of the Central Anatolian Plateau has examples of drainage networks (e.g. Sakarya and Kızılırmak catchments) that are highly disequilibrated (Figure 5a,b). It is generally agreed that long-wavelength knickzones are manifestations of external forcing generated by spatial and temporal patterns of regional uplift. Here, our goal is to use inventories of river profiles to constrain these patterns.

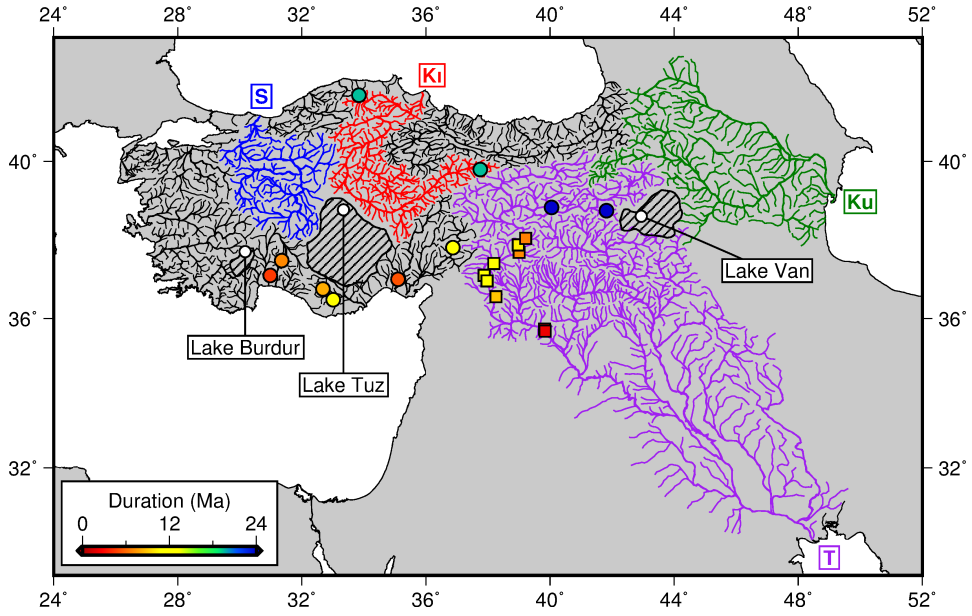

Figure 4. Drainage pattern of Anatolia with loci of independent constraints for calibration. Blue network labeled **S** = Sakarya catchment; red network labeled Kı = Kızılırmak catchment; orange network labeled Ku = Kura catchment; purple network labeled T = Tigris-Euphrates catchment; colored circles/squares = loci of observed uplift/incision rates shaded according to duration.

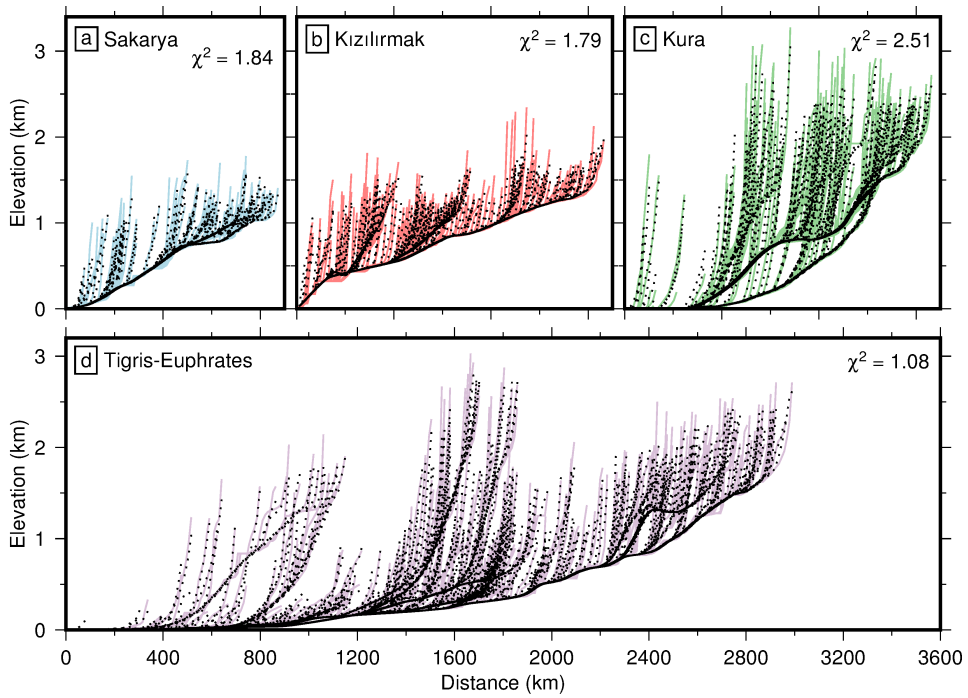

Figure 5. Observed and calculated longitudinal river profiles for major Anatolian catchments. Colored lines = observed river profiles within each catchment; dotted lines = calculated river profiles. (a) Sakarya catchment. (b) Kizilirmak catchment. (c) Kura catchment. (d) Tigris-Euphrates catchment.

3.2 Inverse Modeling Approach

The shape of a longitudinal river profile depends upon the competing interplay between uplift rate, U, and erosion rate, E, so that

$$-\frac{\partial z}{\partial t} = E(x,t) + U(x,t), \tag{3}$$

where x is the distance from the river mouth along a given profile, z is elevation, and t is time before present day. Erosion is usually parametrized using the phenomenological stream power law such that

$$E(x,t) = -vA(x)^m \left(\frac{\partial z}{\partial x}\right)^n + \kappa(x)\frac{\partial^2 z}{\partial x^2}. \tag{4}$$

The first term of this equation describes the headward retreat of steeper portions of the river channel. In this detachment-limited case, v, m and n are erosional constants and A is upstream drainage area [*Howard and Kerby*, 1983; *Whipple and Tucker*, 1999]. The second term describes downward erosion of the channel that is controlled by sedimentary transport. In this transport-limited case, κ represents 'erosional diffusivity' [*Sklar and Dietrich*, 1998; *Whipple and Tucker*, 2002; *Tomkin et al.*, 2003]. The values of v, m, n and κ are poorly known and the subject of considerable debate. Previous studies have found that, at long wavelengths, different values of κ have a negligible influence on the resultant uplift rate histories [*Paul et al.*, 2014; *Rudge et al.*, 2015]. Furthermore, *Paul et al.* [2014], *Czarnota et al.* [2014] and *Rudge et al.* [2015] demonstrate that optimal fits between observed and calculated river profiles are achieved for $n = 1$.

We can therefore simplify the stream power law so that

$$-\frac{\partial z}{\partial t} = -vA(x)^m \left(\frac{\partial z}{\partial x}\right) + U(x,t). \tag{5}$$

This linear kinematic wave equation can be solved using the method of characteristics. Here, we exploit an algorithm developed by *Rudge et al.* [2015] to pose and solve the inverse problem. Uplift values are specified at a discrete set of spatial and temporal nodes, represented by the vector $\mathbf{U}$. The appropriate matrix equation is

$$\mathbf{z} = M\mathbf{U}, \tag{6}$$

where $\mathbf{z}$ is the elevation at different loci along observed river profiles and M is the model matrix that contains the information required to translate any given uplift history into calculated river profiles. This information includes upstream drainage area together with values of the erosional constants. Equation (5) can be inverted to determine $\mathbf{U}$. We use a damped, non-negative least squares approach where we seek to minimize

$$|M\mathbf{U} - z|^2 + \lambda_s^2 |S\mathbf{U}|^2 + \lambda_t^2 |T\mathbf{U}|^2 \quad \text{subject to } \mathbf{U} \geq 0. \tag{7}$$

The non-negativity constraint is imposed to suppress positive and negative oscillations. λ_s and λ_t are spatial and temporal smoothing parameters that control regularization of this problem by penalizing spatial and temporal roughness such that

$$|S\mathbf{U}|^2 = \int_S \int_{t=0}^{t=max} |\nabla U|^2 \; dt \; dS \tag{8}$$

and

$$|T\mathbf{U}|^2 = \int_S \int_{t=0}^{t=max} \left|\frac{\partial U}{\partial t}\right|^2 \; dt \; dS \tag{9}$$

respectively. In this way, hundreds of river profiles can be simultaneously inverted to determine a regional uplift history.

It is necessary to prescribe a topographic starting condition for this inverse model. Miocene marine sedimentary rocks are distributed across portions of Anatolia, which implies that modest topographic relief existed at this time [Figure 1b; Table 1; *Poisson et al.*, 1996; *Hüsing et al.*, 2009; *Cosentino et al.*, 2012; *Schildgen et al.*, 2012a,b; *Cipollari et al.*, 2012, 2013; *Bartol and Govers*, 2014; *Schildgen et al.*, 2014]. This implication is consistent with stable isotopic compositions of sediment samples from continental basins across Central Anatolia, which indicate a lack of significant orographic barriers until Middle Miocene times [*Lüdecke et al.*, 2013; *Schemmel et al.*, 2013]. These observations indicate that negligible topographic elevation is a reasonable starting condition. It is important to point out, however, that other starting conditions could be used.

The inverse algorithm also assumes that the upstream drainage area of each river profile is invariant. In reality, river channels can change their courses, capture events can occur, and drainage divides can migrate [*Willett et al.*, 2014]. Fortunately, upstream drainage area, A, is raised to a fractional power in the stream power formulation (Equation 5). A significant consequence is that uplift histories calculated by inverse modeling are insensitive to substantial (e.g. ±50%) excursions in A [*Paul et al.*, 2014]. Therefore, small-scale capture events generated by drainage divide migration at the backs of catchments are unlikely to significantly affect our results.

A more problematic issue is a major rerouting event, caused by active faulting or switches in regional tilting. However, knickzones that are generated in this way are unlikely to be coherent from catchment to catchment. If so, these events may be recognizable by large values of residual misfit within particular catchments. Active faulting can also laterally displace catchments, affecting the spatial distribution of knickzones and hence the spatial planform of calculated uplift histories. However, estimates of the cumulative offset across the North Anatolian Fault, the dominant tectonic structure, range between 50 and 110 km [*Hubert-Ferrari et al.*, 2002; *Akbayram et al.*, 2016; *Gürsoy et al.*, 2017]. These estimates are small compared to the length scales of regional uplift resolved by inverse modeling.

3.3 Model Calibration

This inverse approach has been used to calculate a regional uplift history of Anatolia from an inventory of 1,844 river profiles (Figures 6 and 7). However, calculated uplift histories are strongly dependent on values of the erosional and smoothing parameters. A total of four parameters must be determined: two erosional constants, v and m, together with two smoothing parameters, λ_s and λ_t. In general, their values are not known *a priori* and instead are calibrated using a combination of the observed river profiles and independent uplift and incision constraints. Unlike m, λ_s and λ_t, v does not directly influence the shapes of river profiles or the spatial pattern of calculated uplift histories. v simply linearly scales the rate of erosion in time and hence the length of calculated uplift histories.

First, we choose the values of m, λ_s and λ_t based upon the amount of residual misfit between observed and calculated river profiles and the roughness of calculated uplift

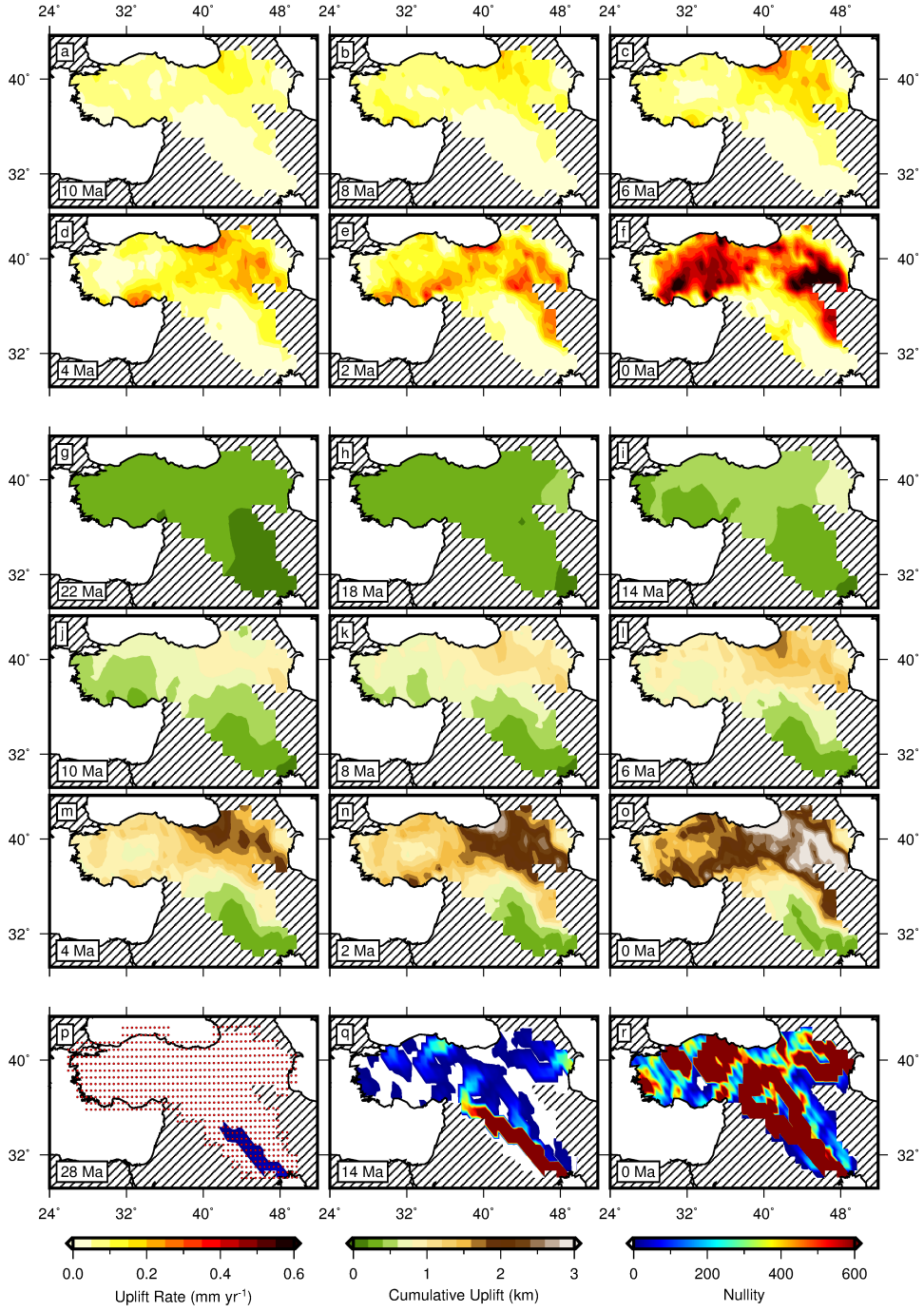

Figure 6. Cumulative uplift history of Anatolia calculated by minimizing misfit between observed and predicted river profiles with $\lambda_s = 1$, $\lambda_t = 3$, $m = 0.45$ and $v = 1.6$. (a)–(f) Spatial pattern of regional uplift rate at selected time steps between 13 Ma and present day. Hatched regions were excluded from inverse model. (g)–(o) Spatial pattern of cumulative uplift at selected time steps between 21 Ma and present day. (p)–(r) Maps showing distribution of non-zero entries (i.e. model coverage) within model matrix, M, at selected time steps.

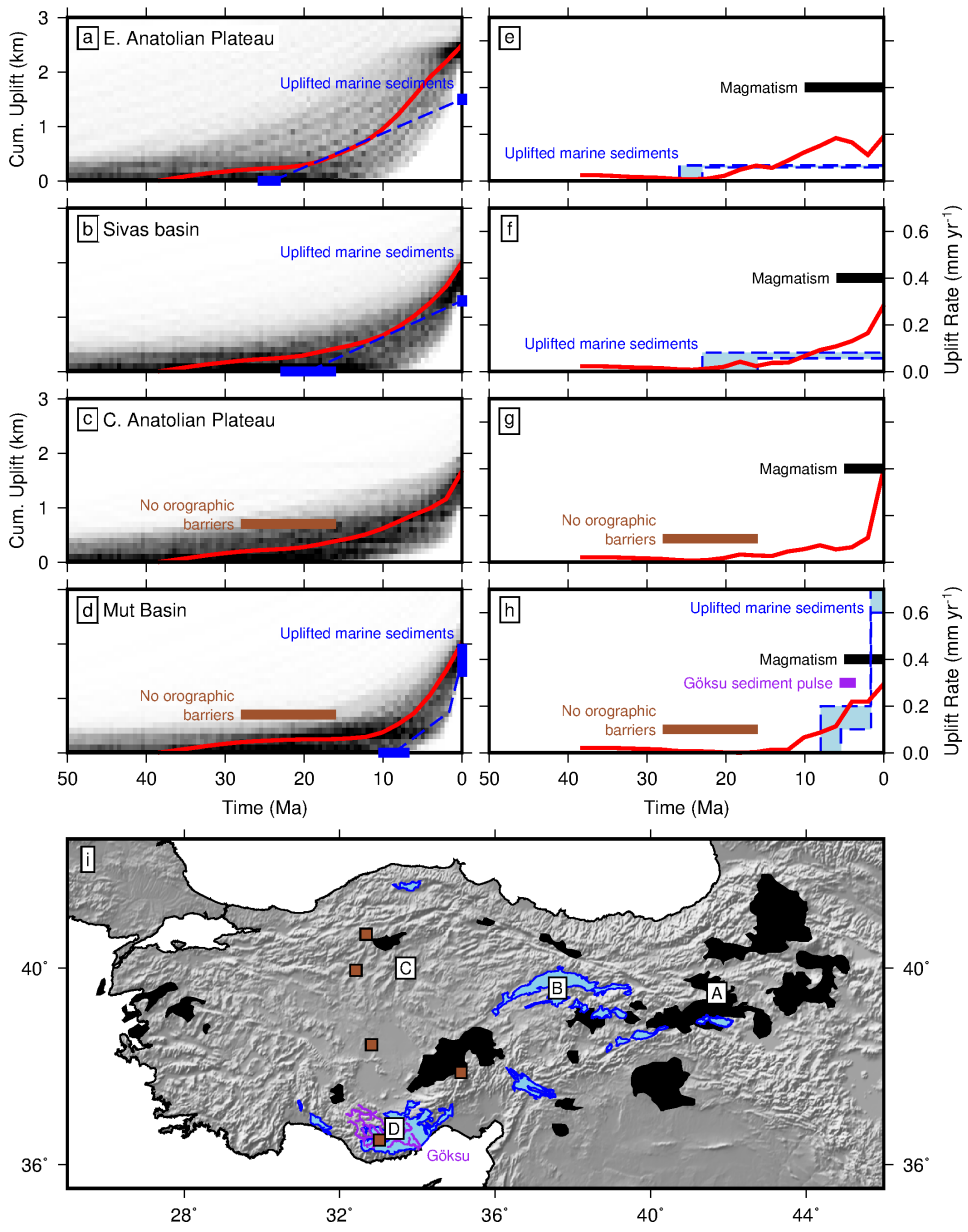

Figure 7. Calculated uplift histories at individual nodes. (a) Cumulative uplift history of Eastern Anatolian Plateau. Red line = optimal cumulative uplift model with $\lambda_s = 0.3$, $\lambda_t = 3\,m = 0.45$ and $v = 1.2$; black/gray pixels = ensemble of smooth models for which χ^2 is less than twice value at global minimum. (e) Uplift rate history of Eastern Anatolian Plateau. Red line = optimal uplift rate model; black bar = Neogene basaltic magmatism. (b) and (f) Silvas basin. Blue bar/dashed lines = marine sedimentary rocks. (c) and (g) Central Anatolian Plateau. Brown bar denotes absence of orographic barrier. (d) and (h) Mut-Erminek basin. Purple bar denotes sedimentary deposition from Göksu catchment. (i) Topographic map showing location of independent constraints. Boxes labeled A–D = loci of individual nodes; blue polygons = uplifted marine sedimentary rocks; black polygons = Neogene volcanic fields; brown squares = loci of sedimentary basins whence samples were taken for stable isotopic study reported by *Lüdecke et al.* [2013]; purple lines = Göksu catchment, for which sedimentary flux history was determined by [*Walsh-Kennedy et al.*, 2014].

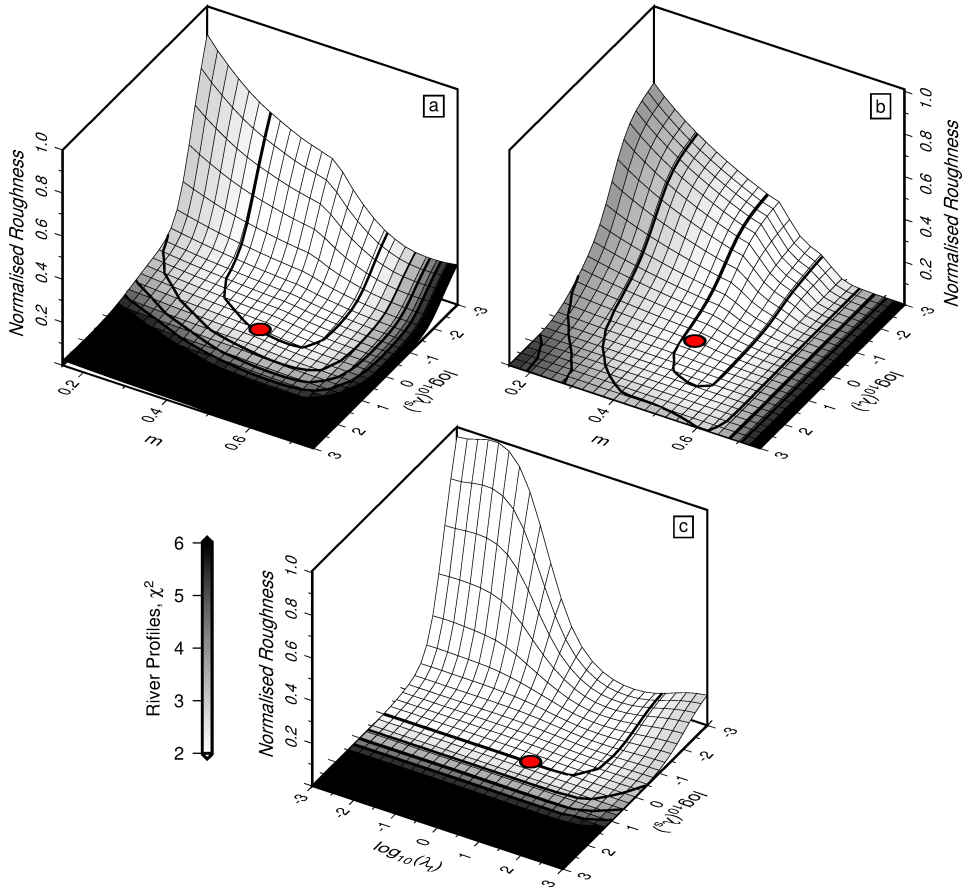

Figure 8. Model misfit and model roughness as function of λ_s, λ_t and m. (a) m–λ_s space. Surface shape represents model roughness where spatial and temporal roughness are combined and normalized between 0 and 1; shading represents misfit between observed and calculated river profiles; red circle = optimal locus in model parameter space. (b) m–λ_t space. and (c) λ_s–λ_t space.

histories. *Richards et al.* [2016] use a similar approach and report significant trade-offs between these three parameters. To assess the effect of these trade-offs on the chosen values of m, λ_s and λ_t, we performed a three parameter sweep. In this sweep, values of m, λ_s and λ_t are simultaneously varied between 0.15 and 0.75, 10^{-3} and 10^3, and 10^{-3} and 10^3, respectively (Figure 8). The minimum misfit between observed and calculated river profiles is obtained for a value of $m \sim 0.45$. The locus of this minimum is not strongly dependent on the degree of spatial or temporal smoothing that is applied, *contra Richards et al.* [2016]. We aim to find values of the two damping parameters that yield the smoothest possible model which still adequately fits the observed river profiles. In this case, we choose $\lambda_s = 1$ and $\lambda_t = 3$ (Figure 8). Examples of river profiles from four catchments calculated using our chosen values of m, λ_s and λ_t are shown in Figure 5.

Secondly, we select the value of v by calibrating against independent observations of uplift rate that are determined from the elevation of emergent marine sedimentary rocks. For example, Neogene deposits containing foraminifera and corals have been identified and biostratigraphically dated in several basins across the region (Figure 1c). At the southern margin of the Central Anatolian Plateau, sediments within the Köprü, Mut-Ermenek and Adana basins were deposited during Tortonian to Calabrian times and are now exposed at elevations of between 1.2 and 2 km [*Cosentino et al.*, 2012; *Schildgen et al.*,

Table 2. Observed and calculated uplift rates.

Location	Lon. (°)	Lat. (°)	Age Range (Ma)	Obs. Rate (mm yr^{-1})	Calc. Rate* (mm yr^{-1})	Ref.
Uplift Constraints						
Sarıkavak	33.65	36.57	1.70 ± 0.04 – 0	0.37 ± 0.02	0.18 ± 0.25 †	a, b
Hacıahmetli	33.60	36.62	1.64 ± 0.02 – 0	0.73 ± 0.01	0.19 ± 0.24 †	a, b
Başyala	32.68	36.77	8.08 ± 0.27 – 0	0.23 ± 0.01	0.16 ± 0.04	c, d
Olukpınar	33.01	36.49	12.75 ± 0.25 – 0	0.13 ± 0.003	0.12 ± 0.03	d
Sarıalan	31.35	37.50	6.94 ± 0.24 – 0	0.22 ± 0.010	0.20 ± 0.08	e
Gebiz	30.98	37.12	4.45 ± 0.85 – 0	0.11 ± 0.03	0.12 ± 0.12	f
Avadan	35.10	37.02	5.25 ± 0.05 – 0	0.10 ± 0.03	0.10 ± 0.13	g
Borehole T-191	35.13	37.01	1.7 ± 0.9 – 0	0.15 ± 0.14	0.12 ± 0.18 †	g
C.E. Sivas	37.75	39.80	19.5 ± 3.5 – 0	0.080 ± 0.015	0.082 ± 0.009	h,i
E. Muş	41.82	38.77	24.0 ± 1.5 – 0	0.062 ± 0.004	0.089 ± 0.015	j
Gevla	40.05	38.85	25.25 ± 2.25 – 0	0.044 ± 0.004	0.068 ± 0.014	j
Avcılar	36.87	37.83	11.35 ± 1.45 – 0	0.072 ± 0.009	0.12 ± 0.05	j
Devrekani	33.84	41.62	19.5 ± 3.5 – 0	0.059 ± 0.011	0.078 ± 0.006	k, l
Incision constraints (Euphrates River)						
Halabiyeh	39.82	35.72	2.72 ± 0.02 – 0	0.040 ± 0.003	0.026 ± 0.0004	m
Zalabiyeh	39.84	35.67	2.12 ± 0.04 – 0	0.021 ± 0.0001	0.023 ± 0.0006	m
Shireen	38.26	36.57	8.9 – 0	0.007	0.025 ± 0.0013	m
Selamet	38.19	37.43	11.40 ± 0.24 – 0	0.033 ± 0.033	0.041 ± 0.0027	n
Özyurt	37.87	37.12	12.68 ± 0.27 – 0	0.027 ± 0.001	0.034 ± 0.0010	n
Asatköyü	37.97	36.98	11.11 ± 0.24 – 0	0.031 ± 0.001	0.032 ± 0.0020	n
Çaylarbaşı	39.01	37.71	7.03 ± 0.16 – 0	0.061 ± 0.001	0.046 ± 0.0053	n
Siverek İskelesi	38.98	37.90	10.24 ± 0.22 – 0	0.045 ± 0.001	0.048 ± 0.0040	n
Saltepe	39.22	38.07	6.70 ± 0.14 – 0	0.073 ± 0.002	0.061 ± 0.0014	n

* Rates are calculated as weighted mean of rates at nodes surrounding point of interest. Uncertainty is taken to be standard deviation of this weighted mean. Note that uplift rates are calculated for v = 1.6 and incision rates for v = 0.9.
† Note that constraints with durations < 2 Ma are below resolution of inverse model and are not included in misfit calculations.
[a – l] References as in Table 1.
[m] *Demir et al.* [2007]. Estimates of incision rate from Ar-Ar dating of incised basalt lava flows.
[n] *Demir et al.* [2012]. Estimates of incision rate from Ar-Ar dating of incised basalt lava flows.

2012a,b; *Cipollari et al.*, 2012, 2013]. Early to Middle Miocene sedimentary rocks at elevations of ∼ 1 km are reported from the Devrekâni basin at the northern margin of the Central Anatolian Plateau [*Tunoğlu*, 1991; *Schildgen et al.*, 2014]. In Eastern Anatolia, marine sediments from the Sivas, Kahramanmaraş, Elazığ and Muş basins were deposited during Aquitanian to Tortonian times and later uplifted to elevations of 1 to 2 km [*Poisson et al.*, 1996; *Hüsing et al.*, 2009]. In this way, average uplift rates over appropriate time intervals can be calculated at specific locations within Anatolia (Table 2). Observed uplift rates can be directly compared with corresponding uplift and incision rates calculated for a range of values of v (Figure 9a and 9b). An optimal value of $v = 1.6 \pm 1.0$ m$^{0.1}$ Ma^{-1} was determined. The upper and lower bounds correspond to values of v that yield χ^2 values that are less than double their values at the global minimum.

In southeastern Anatolia, the Euphrates river has incised a series of flood basalt flows. ^{40}Ar/^{39}Ar dating of these flows permits long-term incision rates to be determined [Figure 4; *Demir et al.*, 2007, 2012]. These calculated local rates help to corroborate our calibration of v. To calculate incision rates for the Euphrates river, we first use a forward model to predict the evolution of its longitudinal profile as a function of time. This forward model solves Equation 5 using an implicit downstream finite-difference scheme for an uplift history previously determined by inverse modeling. Once a suite of river profiles has been calculated, it is straightforward to estimate the amount of vertical incision, z, by using the advective term of the stream power formulation such that

$$z(x,t) = vA(x)\frac{\partial z(x,t)}{\partial x}. \tag{10}$$

Incision rates are calculated for a range of values of v and can then be compared with observed incision rates (Figure 9c and 9d). We obtained an optimal value of $v \sim 0.9^{+0.1}_{-0.2}$ $m^{0.1}$ Ma^{-1}. As before, the upper and lower bounds correspond to values of v that yield χ^2 values that are less than double their values at the locus of the global minimum. This value falls within the range determined using observed and calculated regional uplift rates.

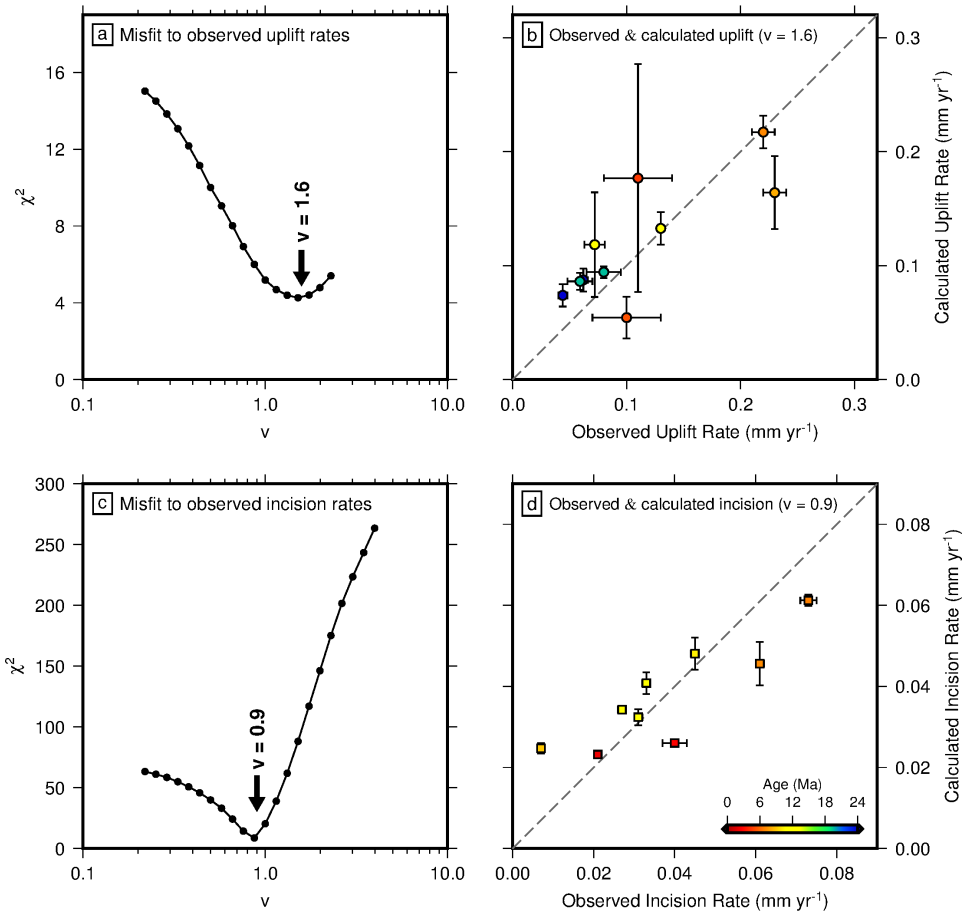

Figure 9. (a) Misfit between observed and calculated uplift rates as function of v for $\lambda_s = 1$, $\lambda_t = 3$, and $m = 0.45$. Global minimum at $v \sim 1.6$ m$^{0.1}$ Ma^{-1}. (b) Calculated uplift rate as function of observed uplift rate for $\lambda_s = 0.3$, $\lambda_t = 3$, $m = 0.45$, and $v = 1.6$ m$^{0.1}$ Ma^{-1}. (c) As (a), for incision rates. Global minimum at $v \sim 0.9$ m$^{0.1}$ Ma^{-1}. (d) Calculated incision rate as function of observed incision rate for $\lambda_s = 0.3$, $\lambda_t = 3$, $m = 0.45$, and $v = 0.9$ m$^{0.1}$ Ma^{-1}.

We emphasise the importance of rigorously testing uplift histories calculated using these chosen values of $m = 0.45$ and $v = 1.6 \pm 1.0$ $m^{0.1}$ Ma^{-1} against a range of additional independent uplift constraints from other locations across Anatolia.

3.4 Cumulative Uplift Histories

Calculated uplift histories that assume $m = 0.45$ and $v = 1.6$ $m^{0.1}$ Ma^{-1} are shown in Figure 6 and in Figure 7. These uplift histories have an acceptable range which reflects permissible upper and lower bounds on m and v. In general, the suite of acceptable models agree with the chronology of uplift events to within $\sim \pm 5$ Ma.

Across the region, negligible uplift occurs before $\sim$ 20 Ma. Subsequently. significant regional uplift commences in the East Anatolian Plateau (Figures 7a,e). This timing is consistent with a transition from marine to continental deposition within the nearby Muş basin [*Hüsing et al.*, 2009]. Uplift rate increases steadily throughout Neogene times, reaching maximum values of 0.15–0.2 mm yr^{-1} by $\sim$ 10 Ma. A total of about 2–2.5 km of cumulative uplift occurs during this period. Onset of regional uplift appears to predate basaltic magmatism by $\sim$ 10 Ma, as noted by *Bartol and Govers* [2014].

After onset of uplift in the East Anatolian Plateau, uplift rapidly migrates westward. At the transition between the Eastern and Central Plateaux, the existence of marine sediments within the Sivas basin suggests that uplift began after $\sim$ 20 Ma. These observations are faithfully reproduced by our inverse model (Figures 7b,f). In agreement with results from the Eastern Anatolian Plateau, uplift rates increase between 15 Ma and the present day to values of $\sim$ 0.2 mm yr^{-1}. Further west, on the Central Anatolian Plateau itself, calculated uplift rates are more constant (Figure 7c,g). They start to increase at $\sim$ 12 Ma, before increasing rapidly from $\sim$ 6 Ma to rates that exceed 0.4 mm yr^{-1} at the present day. These calculated uplift histories are consistent with inferences made from stable isotopic compositions of sediments in continental basins surrounding the Central Anatolian Plateau, which indicate a lack of significant orographic barriers across the region until 15 Ma [*Lüdecke et al.*, 2013]. As observed for the East Anatolian Plateau, magmatism lags the onset of uplift by $\sim$ 10 Ma.

Along the southern edge of the Central Anatolian Plateau, there are important independent constraints for the history of uplift (Figure 7d,h). For example, a suite of uplifted marine sedimentary rocks became emergent at about 8 Ma and record $\sim$ 2 km of regional uplift at rates of up to 0.7 mm yr^{-1} for the last 1.5 Ma [Table 1 *Cosentino et al.*, 2012; *Schildgen et al.*, 2012a,b; *Cipollari et al.*, 2012, 2013]. In our inverse model, uplift begins slightly earlier at 10 Ma and we do not resolve such rapid uplift rates toward the present day. Instead, calculated uplift rates steadily increase to 0.25–0.3 mm yr^{-1} by approximately 5 Ma. This discrepancy is most likely to arise from the temporal smoothing imposed upon our uplift history. Nonetheless, it is worth noting that the culmination of our calculated uplift rates corresponds to a peak in observed sedimentary flux from the Göksu catchment between 5.6 and 3.6 Ma [*Walsh-Kennedy et al.*, 2014]. Along the northern edge of the Central Anatolian Plateau, the inverse model yields an uplift rate of $\sim$ 0.2 mm yr^{-1} after $\sim$ 5 Ma. This value is consistent with the geomorphic observations of *Yıldırım et al.* [2011, 2013] who link this uplift with a large-scale constraining bend of the North Anatolian Fault.

The upstream propagation of kinematic waves of knickzones implies that the length of the potential 'tape recorder' that a river profile represents is strongly dependent upon longitudinal distance and upon the rate of erosion. It is illuminating to consider the spatial and temporal coverage afforded by any given drainage network. This coverage can be gauged by calculating the number of non-zero nodes in the model matrix, M, examples of which are shown in Figures 6p-r. Coverage is excellent for the last $\sim$ 15 Ma. This result implies that the Anatolian drainage network is principally sensitive to Late Neogene uplift signals and that significant features of the uplift history which are discussed here have

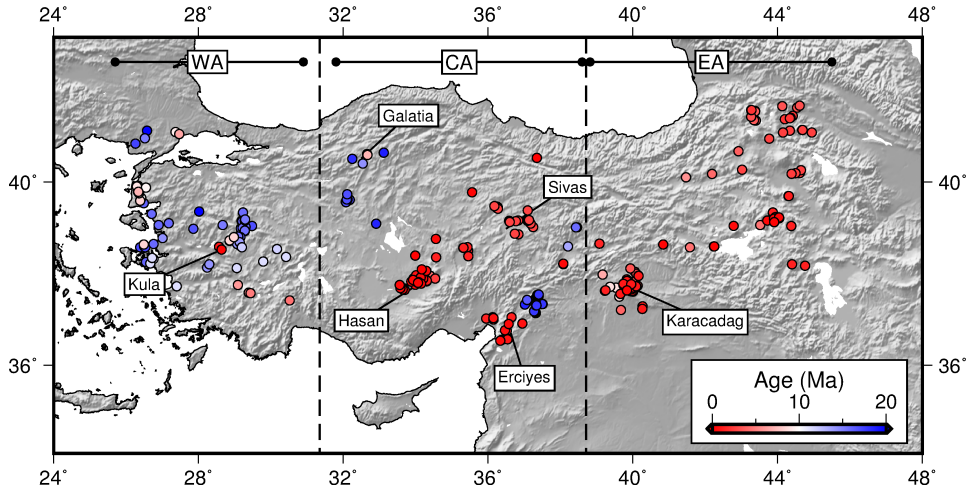

Figure 10. Topographic map of Anatolia showing distribution of Neogene basaltic volcanism. Colored circles = sample locations according to age (see Dataset S3 and references therein); labeled circles refer to locations described in text; WA = Western Anatolia; CA = Central Anatolia; EA = Eastern Anatolia.

been well resolved. An important exception may be the inner Central Anatolian Plateau where endorheic drainage networks around Lake Tuz are omitted from the drainage inventory thus leaving a gap in coverage that persists to the present day.

4 Magmatism

Abundant Neogene magmatism occurs throughout Anatolia and its existence is often linked with geodynamic evolution. A range of processes have been proposed to generate this magmatism that include: subduction of oceanic lithosphere [*Aldanmaz et al.*, 2000; *Ersoy et al.*, 2012]; slab break-off, fragmentation or roll back [e.g. *Keskin*, 2003; *Şengör et al.*, 2003; *Innocenti et al.*, 2005; *Agostini et al.*, 2007; *Reid et al.*, 2017]; extension and delamination of continental lithosphere [e.g. *Pearce et al.*, 1990; *Şengör et al.*, 2008]; and elevated asthenospheric temperatures [e.g. *Şengör et al.*, 2003; *Prelević et al.*, 2012]. Each of these processes could generate different surface expressions and thus modify the evolving landscape in different ways. It is often remarked that there is a significant transition from calc-alkaline to alkaline magmatism in Neogene times. This transition has been interpreted as a shift from subduction zone to intraplate magmatic generation [e.g. *Wilson et al.*, 1997; *Innocenti et al.*, 2005; *Agostini et al.*, 2007; *Keskin*, 2007]. The timing, nature and significance of this transition are poorly understood.

To assess the relative importance of subduction and intraplate processes in generating Anatolian magmatism throughout Neogene times, we have compiled an extensive database of published basaltic samples. These samples have been assigned either radiometric or inferred chronostratigraphic ages (see Data Set S3, and references therein; Figure 10). Major and trace element analyses and/or isotopic measurements of samples with MgO $>$ 5 wt% are presented. For the sake of completeness, this database includes previously unpublished geochemical analyses from Western Anatolia [*Richardson-Bunbury*, 1992; *Paton*, 1992].

4.1 Sample Screening and the Influence of Subduction

The composition of basaltic magmas directly reflects processes involved in their generation and emplacement. Basalts produced by subduction zones are geochemically

distinct from those that are derived from either passively or actively upwelling asthenosphere. Above a subducting slab, the mantle wedge is considerably altered by fluids released by dehydration processes within the slab. Thus the wedge becomes enriched in fluid mobile elements, such as large ion lithophiles (e.g. K, Pb, Ba; *Elliott*, 2003; *Bebout*, 2007). The degree of enrichment can be gauged by taking the ratio of these elements with respect to insoluble equivalents which behave similarly during melting processes (e.g. Nb, Ce). Melts derived from subduction-influenced mantle will therefore have higher values of K/Nb, Pb/Ce and Ba/Nb than those derived from unenriched mantle.

Subduction processes can also modify the isotopic composition of the mantle wedge. Isotopic ratios are not affected by melting or by fractionation processes and the isotopic composition of a sample will directly reflect that of its source material. During formation of continental crust, the upper mantle became depleted in the incompatible elements Rb and Nd, relative to the more compatible Sr and Sm. Subsequently, decay of radioactive ^{87}Rb and ^{147}Sm resulted in concentration of radiogenic isotopes ^{87}Sr within the crust and ^{144}Nd within the upper mantle. Continental crust therefore has high ^{87}Sr/^{86}Sr and low ^{143}Nd/^{144}Nd relative to mantle rocks [*Zindler and Hart*, 1986]. Oceanic sediments are partly derived from the continental crust and so they also acquire elevated ^{87}Sr/^{86}Sr and reduced ^{143}Nd/^{144}Nd values. Incorporation of subducted continental sediments into the mantle wedge therefore raises the ^{87}Sr/^{86}Sr values and lowers the ^{143}Nd/^{144}Nd values of melts generated in subduction zone settings [*Plank and Langmuir*, 1998].

We can exploit these elemental and isotopic systems to track the influence of subduction processes in generating Anatolian magmatism (Figure 11). Here, we use an online compilation to calculate average values for Ocean Island Basalts (OIB; `http://www.georoc.edu`). The mean and standard deviations for OIB samples are shown as gray boxes in Figure 11. There are significant geochemical differences between Western, Central and Eastern Anatolia.

In Western Anatolia, a dramatic transition is evident at about 10 Ma (Figure 11a-e). Prior to 10 Ma, all five systems show a wide range of values, much different to those observed for the majority of OIB samples. The values are consistent with subduction zone magmatism. Since 10 Ma, these values are much more uniform and fall within one standard deviation of the mean observed for OIB samples. This transition is well established and has been linked to the development of a 'slab window' and to the consequent arrival of uncontaminated, sub-slab asthenosphere [*Innocenti et al.*, 2005; *Agostini et al.*, 2007].

In Central Anatolia, there are two distinct magmatic phases (Figure 11f-j). No significant geochemical transition exists between these two phases. The first phase lasted from 20–14 Ma and principally occurred within the Galatia and Erciyes provinces, which are northwest and southeast of the Central Anatolian Plateau, respectively. The second phase lasted from about 5 Ma to the present day and occurs in central and eastern Central Anatolia (e.g. Hasan, Sivas). Throughout Neogene times, the range of values for each of the subduction-sensitive parameters is significantly lower than that observed within subduction zone settings and within Western Anatolia prior to 10 Ma. However, they exhibit a modest subduction zone signature compared with the majority of OIB samples.

Similar values for each of the subduction-sensitive parameters are obtained for Eastern Anatolia where magmatism occurs continuously from $\sim$ 12 Ma (Figure 11k-o). The absence of a switch from subduction-influenced to intraplate-style magmatism in Neogene times for Central and Eastern Anatolia does not agree with the results of several earlier studies [*Wilson et al.*, 1997; *Keskin*, 2007]. In order to mitigate sensitivity to the effects of fractionation and contamination, we only include samples with MgO > 5 wt%. These previously described switches rely upon samples that do not pass our chosen cut-off value of MgO. It is difficult to assess the relevance of these more fractionated samples as a guide to the composition of the mantle source. Our focus is exclusively upon high MgO basalts

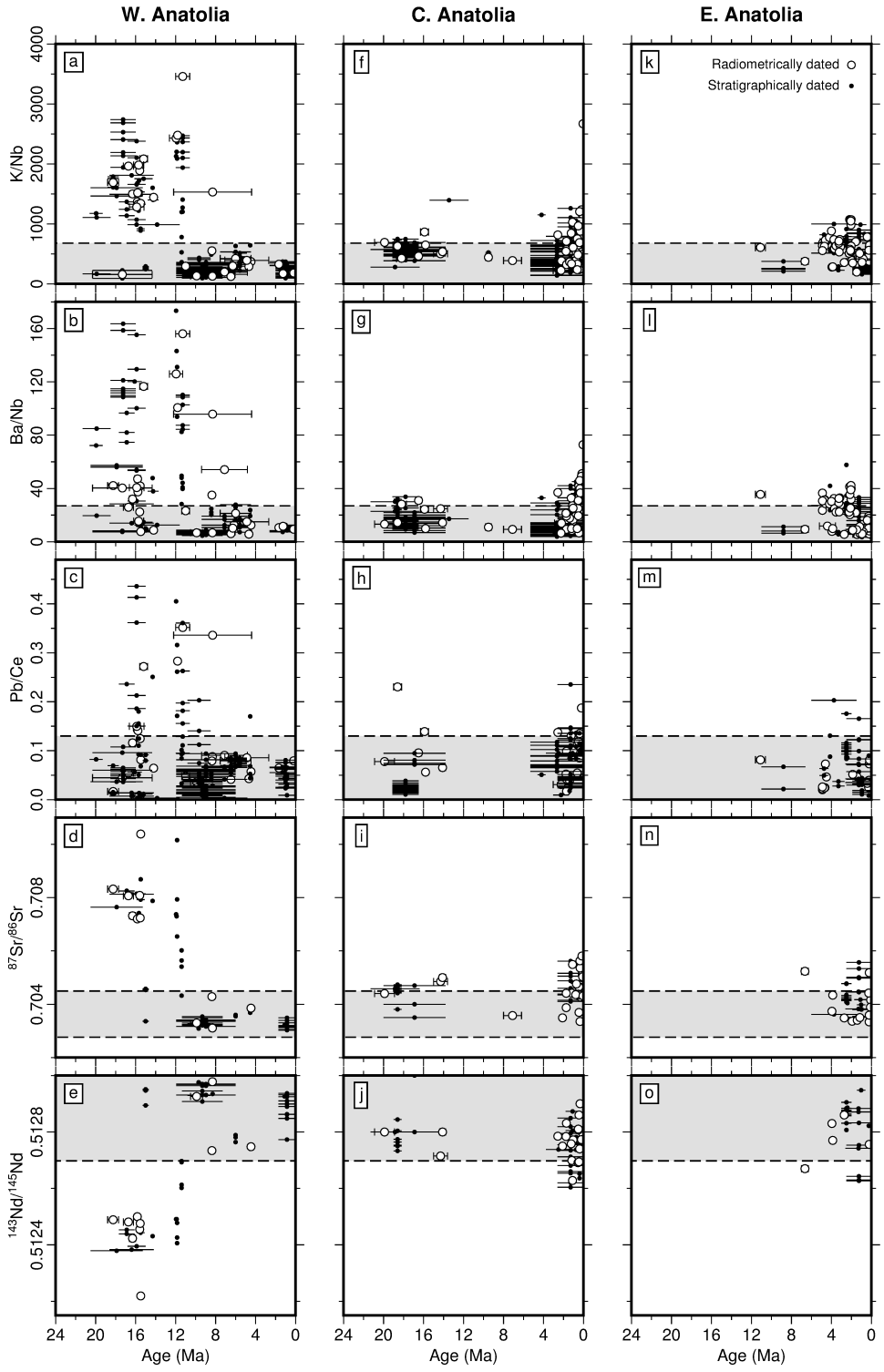

559 **Figure 11.** Geochemical analyses of basaltic volcanism from Western, Central and Eastern Ana-
560 tolia as function of radiometric age. White circles with horizontal bars = radiometrically dated sam-
561 ples $\pm 1\sigma$; black circles with horizontal bars = chronostratigraphically dated samples $\pm 1\sigma$; gray boxes
562 with dashed lines = mean and standard deviation of ocean island basalts from GEOROC database (OIB;
563 `http://www.georoc.edu`). In Western Anatolia, note dramatic change in composition at $\sim$ 10 Ma.

which means that this regional Neogene shift away from subduction-influenced magmatism in Central and Eastern Anatolia is less obvious.

$^{87}Sr/^{86}Sr$ and $^{143}Nd/^{144}Nd$ are independent systems that can be combined to more closely constrain the nature of the putative source region. Several different mantle reservoirs can been defined within $^{87}Sr/^{86}Sr$–$^{143}Nd/^{144}Nd$ space. The isotopic composition of primitive mantle is thought to be that of the bulk Earth, which has a present-day average composition of $^{87}Sr/^{86}Sr = 0.7047$ and $^{143}Nd/^{144}Nd = 0.51265$ [Figure 12; *Philpotts and Ague*, 2009]. Fractional melting of primitive mantle raises the $^{143}Nd/^{144}Nd$ ratio and lowers the $^{87}Sr/^{86}Sr$ ratio of the source rock. Reservoirs that are thought to represent uncontaminated mantle, including those invoked as potential sources for OIB-style magmatism (e.g. CMR: common mantle reservoir; HIMU: high-μ reservoir; FOZO: focal zone reservoir), lie along a 'mantle array' between bulk Earth and a significantly depleted endmember known as Depleted MORB Mantle [DMM; Figure 12; *Zindler and Hart*, 1986; *Hart et al.*, 1992; *Stracke et al.*, 2005; *Lustrino and Wilson*, 2007]. Fractional melting of primitive mantle also generates enriched products. Examples include reservoirs that are thought to be representative of lower crust (e.g. EM1), upper crust (e.g. EM2), or oceanic sediments (e.g. EMS) have higher values of $^{87}Sr/^{86}Sr$ and lower values of $^{144}Nd/^{145}Nd$, relative to the bulk Earth [*Zindler and Hart*, 1986; *Klaver et al.*, 2015].

In general, Anatolian basaltic rocks lie along a simple binary mixing line between a partially depleted OIB-like source (e.g. CMR, HIMU, FOZO) and an enriched oceanic sediment or upper crustal source (e.g. EM2, EMS; Figure 12). There is no requirement to invoke significant depletion of the mantle source or contamination by lower crustal material. K/Nb, Pb/Ce and Ba/Nb ratios all correlate well with the relative importance of the EM2/EMS sources, implying that variations in the isotopic composition of Anatolian basaltic rocks are primarily controlled by the degree of contamination by subducted oceanic sediments. At high values of $^{143}Nd/^{144}Nd$, there is a systematic shift to higher values of $^{87}Sr/^{86}Sr$ from west to east. To assess the potential influence of contamination by continental crust, we calculate mixing lines between the least enriched basaltic sample and Neoproterozoic basement material from Western Anatolia [Augen gneiss; *Gürsu*, 2016]. The observed shift to higher $^{87}Sr/^{86}Sr$ values in Eastern Anatolia is consistent with up to 10% of crustal contamination and probably reflects increasing crustal thickness from west to east.

In Western Anatolia, basaltic samples span the full range of isotopic compositions from OIB-like mantle to oceanic sediments (Figure 12a,d). As observed on Figure 11, there is a clear age progression, with the degree of enrichment decreasing towards the present day. The most recent basaltic products fall entirely within the observed ranges of uncontaminated mantle reservoirs and require no enrichment by subduction. In Central and Eastern Anatolia, samples require significantly less enrichment than the older (i.e. pre-10 Ma) samples from Western Anatolia (Figures 12b,e and c,f). However, unlike the youngest Western Anatolian rocks, all samples are enriched to some degree. This enrichment could reflect residual/continued contamination of the asthenosphere by subduction processes or melting of previously contaminated lithospheric material.

4.2 Mantle Potential Temperatures

It is evident that subduction processes are not responsible for the generation of basaltic magmatism for the last 10 Ma in Western Anatolia and during Neogene times in Central and Eastern Anatolia. Instead, melting of an OIB-like or partially enriched source region could be accounted for by passive upwelling caused by lithospheric extension, by lithospheric delamination or slab fragmentation, or by elevated asthenospheric temperatures. We investigate these potential mechanisms by employing two independent schemes for estimating mantle potential temperature, T_P. First, we employ the major element thermobarometer developed by *Plank and Forsyth* [2016]. Secondly, inverse modeling of rare

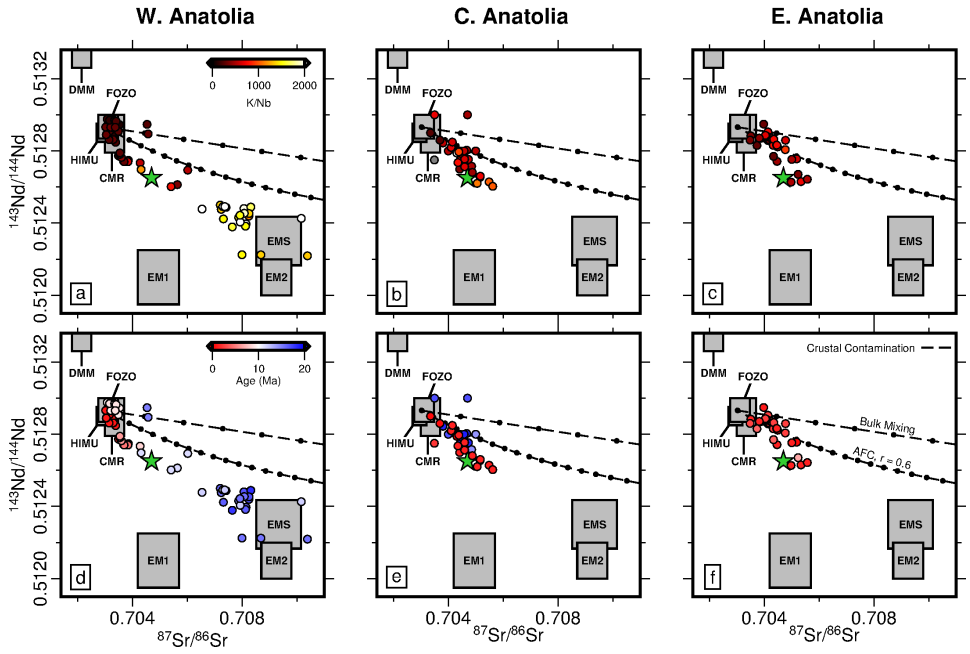

Figure 12. Isotopic compositions of mafic volcanism from Anatolia. (a) $^{143}Nd/^{144}Nd$ plotted as function of $^{87}Sr/^{86}Sr$ for Western Anatolia. Circles are colored according to K/Nb ratio; green star = bulk Earth composition [*Philpotts and Ague*, 2009]; labeled gray polygons = mantle reservoirs where HIMU is high-μ mantle, FOZO is the focal zone reservoir; DMM is depleted MORB mantle; EM1/EM2 is enriched mantle 1 and 2 [*Zindler and Hart*, 1986], CMR is common mantle reservoir [*Lustrino and Wilson*, 2007], EMS is eastern Mediterranean sediments [*Klaver et al.*, 2015]; upper/lower dashed lines = bulk mixing/assimilation and fractional crystallization (AFC) trends between most primitive basalts and average composition of augen gneisses that are representative of Anatolian basement [*Gürsu*, 2016]. AFC trends are calculated using *DePaulo* [1981] mixing equations. (b) Isotopic plot for Central Anatolia. (c) Isotopic plot for Eastern Anatolia. (d)–(f) Isotopic plots where circles are colored according to radiometric age.

earth element concentrations is carried out [*McKenzie and O'Nions*, 1991]. Both of these methods can be used to model high-Mg basalts generated from peridotitic mantle and account for fractionation of olivine. We have identified a subset of samples with MgO > 8.5 *wt%* that are deemed suitable for modeling and we focus on the youngest, post-10 Ma, phase of magmatism.

It is useful to compare estimates of T_P with the potential temperature of ambient convecting mantle. Estimates of this ambient value vary depending upon methodology [e.g. *Katsura et al.*, 2004; *Herzberg et al.*, 2007; *Dalton et al.*, 2014; *Matthews et al.*, 2016]. Throughout the following section, we exploit the adiabatic melting models of *McKenzie and Bickle* [1988] and *Katz et al.* [2003]. The value of T_P required to produce 7.1 km of oceanic crust by adiabatic decompression melting using these parameterizations is 1310–1335 °C. We conclude that a suitable reference value of T_P for ambient mantle is ~ 1320 °C.

4.2.1 Major Element Thermobarometry

Building upon the pioneering work of *Lee et al.* [2009], *Plank and Forsyth* [2016] developed parameterizations of source temperature and pressure using an extensive compilation of experimental melt equilibration datasets. Their approach exploits the fact that partitioning of major elements during melting is dependent on pressure and temperature. First, observed major element compositions of high-Mg basalts are corrected for olivine fractionation to estimate primary melt compositions. Olivine in equilibrium with melt is incrementally added until melt compositions reach equilibrium with mantle that has an assumed olivine forsterite content. For each of the basaltic samples, we back-calculate to an Mg number of the melt given by Mg# = Mg/Mg + Fe = 0.9 in olivine. This value of Mg# is considered to be a reasonable average value for partially depleted mantle [*Lee et al.*, 2009]. This correction, together with the pressure and temperature calculations, are also dependent upon the ratio of Fe^{3+} to Fe^{2+}, and upon the water content of the melt.

Once primary melt compositions have been estimated, temperature, T, and pressure, P, are calculated using a parameterization so that

$$T\ (K) = 1264.5 + 7.85(Mg_4Si_2O_8) + \frac{8545}{Si_4O_8} - 5.96(Al_{16.3}O_8) - \Delta T_{H_2O} - \Delta T_{CO_2}, \quad (11)$$

and

$$P = \frac{ln(Si_4O_8) - 4.045 + 0.0114(Fe_4Si_2O_8) + 0.00052(Ca_4Si_2O_8)^2 + 0.0024(Mg_4Si_2O_8)}{-336.3T^{-1} + 0.0007T^{1/2}}, \quad (12)$$

where

$$\Delta T_{H_2O} = 40.4(H_2O) - 2.97(H_2O)^2 + 0.0761(H_2O)^3. \quad (13)$$

Compositional components are reported in mole%, as defined by *Lee et al.* [2009], with the exception of H_2O which is reported in wt%. A correction is applied to any samples which initially give equilibrium pressures in excess of 2 GPa in order to account for the effects of undersaturated CO_2. Thus

$$\text{if } P > 2.0 \text{ GPa, then } \Delta T_{CO_2} = \frac{SiO_2 - 50.3}{0.128}, \text{ else } \Delta T_{CO_2} = 0, \quad (14)$$

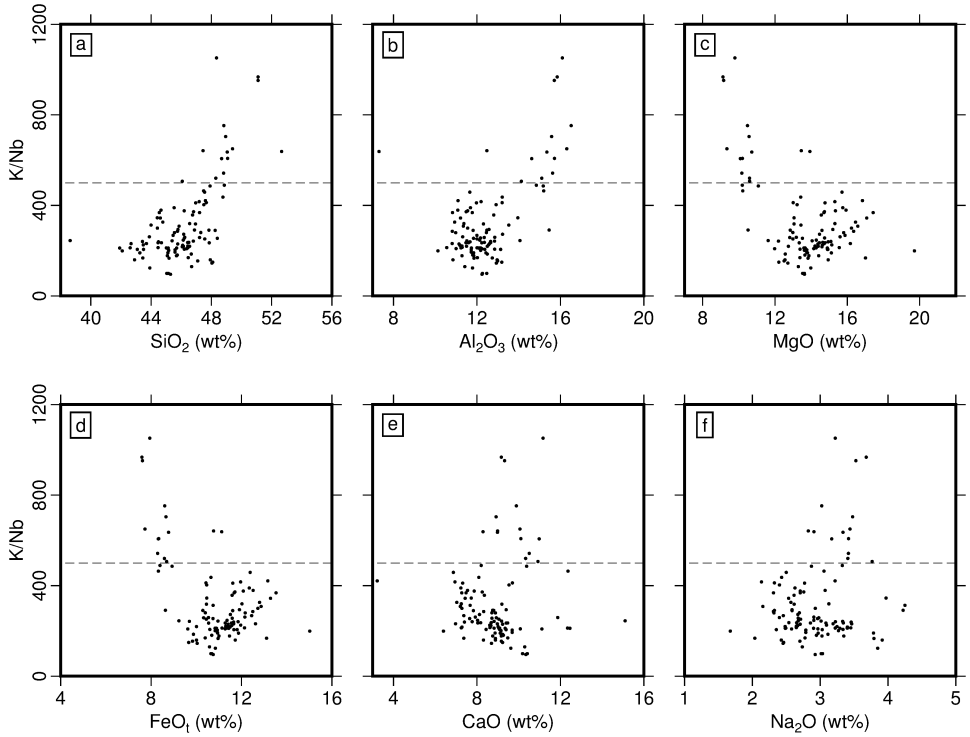

Figure 13. K/Nb as a function of major elements for Anatolian basalts where Mg > 8.5 wt%. (a) K/Nb ratio plotted as function of SiO_2. Dashed line indicates K/Nb = 500. (b) K/Nb ratio plotted as function of Al_2O_3. (c) K/Nb ratio plotted as function of MgO. (d) K/Nb ratio plotted as function of FeO_t. (e) K/Nb ratio plotted as function of CaO. (f) K/Nb ratio plotted as function of Na_2O. Major element concentrations are corrected for olivine fractionation in order to estimate primary melt compositions [*Lee et al.*, 2009].

where SiO_2 is in wt%. For these particular samples, pressure is then recalculated using the revised temperature.

Temperature and pressure estimates clearly depend upon variations in major elemental concentrations. Changes in melt composition can also arise as a result of heterogeneities in source composition and mineralogy. We have already highlighted the fact that K/Nb can be used as a proxy for enrichment by subduction processes across Anatolia. Two distinct populations are identified in major element-K/Nb space (Figure 13). For K/Nb values greater than $\sim$ 500, samples generally shift to higher values of SiO_2, Al_2O_3 and CaO, and to lower values of MgO and FeO_t (i.e. combined FeO and Fe_2O_3). The magnitudes of these shifts are unlikely to be caused by subduction enrichment. Rather, they probably reflect distinct equilibration conditions for both populations. These trends act consistently to reduce the temperature and pressure estimates for high K/Nb samples. Therefore, when estimating mantle potential temperatures beneath Anatolia, these two populations are separately treated.

Thermobarometric calculations for Western, Central and Eastern Anatolia are shown in Figure 14. These results are strongly dependent upon the value of $Fe^{3+}/\Sigma Fe$, which is controlled by oxidation state, and upon the assumed water content. In Anatolia, direct measurements of $Fe^{3+}/\Sigma Fe$ and of water concentrations within melts are scarce. Globally, it is observed that $Fe^{3+}/\Sigma Fe$ varies between 0.1 for mid-ocean ridge basalts (MORB) and 0.3 for arc settings [*Cottrell and Kelley*, 2011; *Brounce et al.*, 2014]. Average estimates for the Basin and Range province of western North America are $\sim$ 0.2 [*Plank and*

Forsyth, 2016]. We assume that this value is appropriate for Anatolia, given the tectonic similarities of these regions— a combination of recently active subduction processes and subsequent generation of basaltic melts with OIB affinities [*Fitton et al.*, 1991; *Kempton et al.*, 1991]. H_2O is known to scale with Ce for MORB samples so that H_2O/Ce = 200 ± 100 [*Michael*, 1995; *Dixon et al.*, 2002]. The results shown in Figure 14a-c assume that $Fe^{3+}/\Sigma Fe = 0.2$ and that $H_2O/Ce = 200$.

In order to relate these results to mantle potential temperature, T_P, we have fitted adiabatic decompression melting paths to calculated equilibration temperatures and pressures. Melting paths are determined using the anhydrous parameterization of *Katz et al.* [2003], assuming a modal clinopyroxene value of 0.15. The misfit between melting paths and calculated equilibration conditions is calculated using a least squares approach, where temperature and pressure are normalized by the respective uncertainties ± 39 °C and ± 0.24 GPa, quoted by *Plank and Forsyth* [2016].

Two distinct magmatic populations exist in Central and Eastern Anatolia: calculated equilibration pressures and temperatures for high K/Nb samples are consistently colder and shallower than those for low K/Nb samples. The latter samples lie along regionally consistent melt paths that require varying mantle potential temperatures. Temperatures are highest in Eastern Anatolia and decrease toward the west. Best-fit melting paths for low K/Nb samples that lie above the solidus, along with a range of paths that can equally fit these date, are shown in Figure 14a-c. These melting paths correspond to mantle potential temperatures of $T_P = 1350^{+30}_{-30}$ °C for Western Anatolia, $T_P = 1380^{+40}_{-30}$ °C for Central Anatolia, and $T_P = 1400^{+90}_{-40}$ °C for Eastern Anatolia. In general, the top of the melting column is at about 50 km depth.

The quoted upper and lower bounds correspond to values of T_P that yield misfit values that are less than twice those at the global minima. Average melt fractions along these melting paths are 4.1 ± 2.0 %, 6.8 ± 2.3 % and 7.6 ± 5.0 % for Western, Central and Eastern Anatolia, respectively. In contrast, the high K/Nb population does not lie along consistent melt paths. Instead, it clusters near the solidus at depths shallower than 50 km. We suggest that the samples from this population probably reflect melting of, or contamination by, lithospheric material enriched during earlier episodes of subduction. This more complicated evolution means that fitting adiabatic decompression melting paths is not reasonable.

To assess the influence of uncertainties in water content and oxidation state, we repeated the modeling procedure for the full range of globally observed values. The revised results for each region are shown in Figure 14d-f. Higher values of $Fe^{3+}/\Sigma Fe$ and H_2O/Ce tend to reduce our estimates of potential temperatures. For Western Anatolia, calculated temperatures through much of the parameter space are at or below that of ambient mantle For the chosen values of $Fe^{3+}/\Sigma Fe = 0.2$ and $H_2O/Ce = 200$, the estimated potential temperature is within the range of uncertainty error of that for ambient mantle. For Central Anatolia, our estimates of mantle potential temperature approach those for ambient mantle for the highest values $Fe^{3+}/\Sigma Fe$ and H_2O/Ce. For Eastern Anatolia, excess temperatures are required for all reasonable values of $Fe^{3+}/\Sigma Fe$ and H_2O/Ce.

4.2.2 Inverse Modeling of Rare Earth Element Concentrations

Partitioning of rare earth elements (REEs) is sensitive to both the depth and degree of melting. During mantle melting, the REEs are incompatible so that their abundance is reduced with increasing melt fraction. Compatibility of the heavy REEs is dependent upon the aluminous phase that is present. Since there is a pressure-dependent transition from spinel to garnet in the uppermost mantle, the relative abundance of light and heavy REEs is dependent upon the depth of melting. Heavy REEs are more compatible in garnet than in spinel so that melting of garnet-bearing peridotite will lead to a relative depletion of these elements. *McKenzie and O'Nions* [1991] developed the INVMEL algorithm for

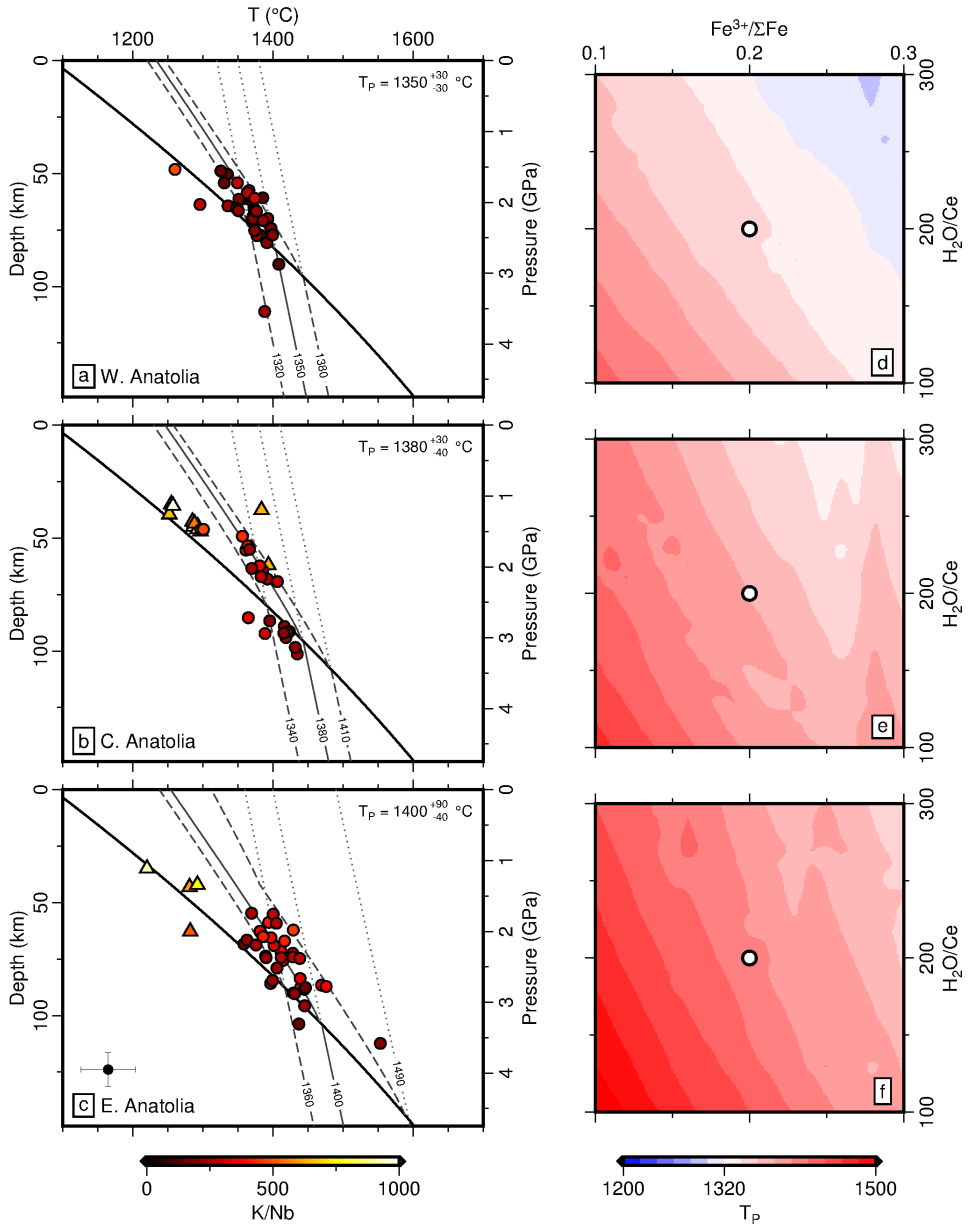

Figure 14. Thermobarometric calculations. (a) Temperature plotted as function of depth/pressure. Colored circles = equilibration pressures and temperature estimates determined for mafic samples (MgO > 8.5 wt%) from Western Anatolia with K/Nb < 500 using $Fe^{3+}/\Sigma Fe = 0.2$ and $H_2O/Ce = 200$; black line = anhydrous solidus; gray line = best-fit melt pathway; dashed gray lines = minimum and maximum melt pathways; dotted gray lines = adiabatic gradients corresponding to loci of intersection between melt pathways and anhydrous solidus [*Katz et al.*, 2003]; optimal value of potential temperature, T_p, given in top right-hand corner. (b) Estimates for Central Anatolia. Triangles = samples with K/Nb > 500. (c) Estimates for Eastern Anatolia. (d)–(f) Distribution of potential temperatures obtained by varying $Fe^{3+}/\Sigma Fe$ and H_2O/Ce. In each case, white circle = values used for thermobarometric calculations shown in panels (a)–(c).

adiabatic decompression of peridotite, which exploits these relationships by inverting REE distributions in order to calculate melt fraction as a function of depth.

The INVMEL scheme inverts observed REE concentrations by summing fractional melts over incremental depths to determine cumulative melt fraction as a function of depth. Mantle potential temperature is then estimated by comparing resultant melt-fraction-with-depth distributions to parameterized mantle adiabats. Spinel-garnet transition-zone depths are fixed in advance. Here, we have chosen a transition at 63–72 km, in agreement with the thermodynamic modeling results of *Jennings and Holland* [2015]. The lower limit of their transition zone has been increased from 68.1 km to 72 km in order to stabilize the inversion procedure. We estimate source compositions for each inversion run by mixing components of depleted (i.e. $\epsilon\mathrm{Nd} = 10$) and primitive (i.e. $\epsilon\mathrm{Nd} = 0$) mantle compositions to match the observed average value of ϵNd for each sample suite [see Dataset S3 for further details; *McKenzie and O'Nions*, 1991]. Partition coefficients are calculated using the parameterization of *Blundy and Wood* [2003]. Melt paths are specified at 3 km depth increments and melting is assumed to cease at the base of the lithospheric column. The inverse model iteratively calculates melt compositions for different melt-fraction-with-depth curves. The root mean square (rms) misfit between calculated and observed compositions is minimized using Powell's conjugate gradient search algorithm [*Press et al.*, 1992]. Lithospheric thickness and the starting melt-fraction-with-depth model are varied until a best-fit to the observed REE distribution is achieved for a smooth output melt-fraction-with-depth curve.

Once a best-fitting curve of melt fraction as a function of depth has been determined, a forward model is produced for the complete element suite in order to test the extent to which the optimal result matches major and other trace element observations. Olivine fractionation does not significantly affect REE concentrations within the melt. It does, however, contribute to variations in Mg and Fe concentrations, which results in a disparity between observed and modeled values of these elements. The amount of olivine addition required to explain this disparity is straightforward to calculate. The final melt fraction is given by $1/(1 - F)$, where F is the estimated weight fraction of crystallized material. Starting models, best-fit models, and fractionation-corrected models are all presented in Figure 15. Inverse modeling of enriched samples (i.e. K/Nb > 500) using simple melting models results in larger misfits to observed trace element concentrations. Acceptable fits can only be achieved with a strongly modified mantle source, the characterization of which introduces a significant degree of uncertainty. We therefore omit samples with K/Nb > 500.

In Western Anatolia, very low melt fractions (i.e. < 2%) are required to replicate high REE concentrations. This melting must occur within both the garnet and spinel stability fields. Consequently, the resultant melting path spans a broad depth range and does not track a calculated adiabat. Optimal fits to observed REE concentrations are achieved by using a lithospheric thickness of 57 km. At these depths, low melt fractions require potential temperatures of less than ~ 1340 ° C (Figure 15a-c). Observed REE concentrations decrease eastward, so that calculated melt fractions increase to 3.1% for Central and 4.7% for Eastern Anatolia. The best-fitting lithospheric thicknesses are 61 km and 62 km, respectively. At shallow depths, melting paths approximately follow adiabats that correspond to mantle potential temperatures of ~ 1355 °C and ~ 1370 °C (Figure 15d-i).

In all three regions, the majority of observed REE and trace element concentrations can be accurately matched. In Central and Eastern Anatolia, the forward model tends to overpredict concentrations of Cs, Rb and Ba. These elements are highly soluble and so any discrepancies may reflect leaching during the weathering process. REE concentrations are far less sensitive to the weathering process, which suggests that the results of inverse modeling are less affected. The forward model also consistently underpredicts concentrations of Ta and Nb, possibly as a consequence of uncertainties in partition coefficients and/or source composition for these particular elements. In general, calculated melting

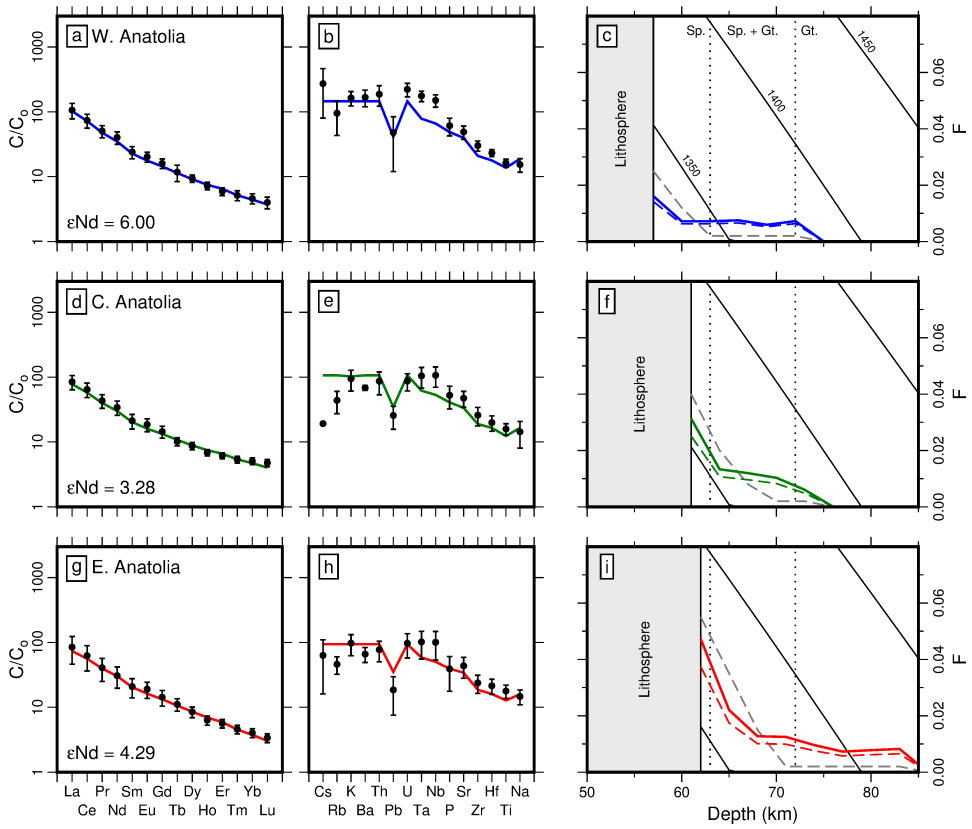

Figure 15. Inverse modeling of rare earth element distributions. (a) Western Anatolia. Black circles with error bars = average observed concentrations of rare earth elements normalized with respect to mixed mantle source $\pm 1\sigma$; blue line = best-fitting calculated concentrations obtained by inverse modeling. (b) Black circles = trace element concentrations; blue line = predicted concentrations; (c) Cumulative melt fraction, F, as function of depth. Dashed blue line = distribution of F obtained using calculated concentrations of rare earth elements shown in panel (a); solid blue line = same corrected for fractionation of olivine; dashed gray line = starting distribution of F; shaded box = lithosphere; vertical dotted lines = spinel-garnet (Sp-Gt) transition zone; solid labeled lines = potential temperature adiabats [*McKenzie and Bickle*, 1988]. (d)–(f) Central Anatolia. (g)–(i) Eastern Anatolia.

paths exhibit long, low melt-fraction tails because observed REE concentrations require small-degree melting within the garnet stability field before the onset of adiabatic decompression at shallower depths. Similar low melt fraction tails have been reported for the Potrillo Volcanic Field of North America and for the Galápagos islands [*Thompson et al.*, 2005; *Gibson and Geist*, 2010].

4.2.3 Magmatic Insights

Both modeling techniques show that there is an asthenospheric temperature gradient across Anatolia. Temperatures increase by ~ 50 °C from west to east and the top of the melting column for low K/Nb samples lies at a depth of about 60 km. Although regional patterns in melt fraction and potential temperature estimates from both approaches generally agree, there are systematic differences in their optimal values. Melt fractions and temperatures estimated using the *Plank and Forsyth* [2016] parameterization are consistently 2–4 % and 10–30 °C higher than those calculated using the INVMEL algorithm. We acknowledge that both techniques are subject to different uncertainties and approximations that can affect estimates of melt fraction and mantle T_P.

A general assumption in both cases is that melts are derived from unenriched lherzolitic mantle. Anatolia has undergone a complex and protracted geodynamic history. Long-lived subduction throughout closure of the Neotethys Ocean has probably significantly altered the composition of the underlying mantle, as is manifest, for example, by compositions of Early to Middle Miocene magmatic rocks exposed in Western Anatolia. Our analysis suggests that after ~ 10 Ma, subduction processes have had a limited influence on basaltic compositions with the exception of some partially enriched samples that are thought to be derived from melting of, or contamination by, enriched lithospheric material. By excluding samples with values of K/Nb > 500, we are confident that the assumed mantle composition is a reasonable one. However, it is important to note that concentrations of REEs are more sensitive to source enrichment than major elements due to their lower concentrations. For inverse modeling, an underestimation of REE concentrations within the source region results in underprediction of melt fraction and asthenospheric T_P. This underprediction probably accounts for at least some of the difference between the results of major element thermobarometry and REE inverse modeling.

Our methods for estimating mantle T_P generally rely on anhydrous melting models. In reality, source materials are likely to contain at least a small amount of water. Source water concentrations are not well known but, given relatively low concentrations within the melts (~ 1.5 ± 0.8 wt%), they are unlikely to be greater than ~ 0.1 ± 0.05 wt% for H_2O/Ce = 200 at 5% melting. This value is consistent with estimates from OIBs and is at the low end of estimates for a subduction-modified mantle wedge [i.e. ~ 0.075 wt% and 0.1-1 wt%, respectively; *Dixon et al.*, 2002; *Karato*, 2011]. It is possible to incorporate hydrous melting into parameterizations of mantle melting [e.g. *Ghiorso et al.*, 2002; *Katz et al.*, 2003; *Langmuir et al.*, 2006; *Hirschmann*, 2010; *Kelley et al.*, 2010]. The addition of water shifts the solidus to greater depths. We note that hydrous melting parameterizations vary significantly and are often only constrained by experimental data limited to pressures equivalent to depths < 60 km [*Katz et al.*, 2003]. Due to these significant uncertainties in the parameterization of hydrous melting, we prefer to focus upon anhydrous melting models.

We require melting models to relate estimates of melt equilibration pressure and temperature derived from major element thermobarometry to T_P. Incorporating hydrous melting would require higher T_P melt paths to fit the melt equilibration data. If there are significant amounts of water in the source region, our estimates of T_P are minima. Using the hydrous melting model of *Katz et al.* [2003] with 0.1 wt% of water in would result in T_P estimates that are up to ~ 40 °C hotter. Due to the concave-upward shape of the solidus, this effect becomes greater as temperature increases. In this way, the observed

gradient of potential temperature across Anatolia would be steepened by incorporating hydrous melting. Unlike the major element parametrization, the INVMEL algorithm explicitly incorporates a melting model as part of the calculation. In this case, addition of water will lower the calculated value of T_P since melting will necessarily occur deeper and at lower temperatures. Nonetheless, water is extremely incompatible and readily enters the melt so that its supply is rapidly diminished. The cooling effect is therefore greater at lower melt fractions, which means that the observed gradient of T_P across Anatolia is likely to be preserved by incorporating hydrous melting.

A potential challenge in relating melt equilibration conditions to asthenospheric potential temperature identified by *Plank and Forsyth* [2016] concerns the pooling and conductive cooling of melts at the base of the lithosphere. These authors have invoked this phenomenon to account for melt equilibration estimates at locations from western North America that lie parallel to the solidus. Distributions of our melt equilibration estimates for low K/Nb samples are significantly steeper than the solidus and can be approximated by adiabatic decompression melting paths. Therefore, there is no requirement to invoke conductive cooling. If a degree of conductive cooling has affected the estimated melt equilibration conditions, our T_P estimates would be minima. In contrast, the majority of high K/Nb samples presented here do cluster close to the solidus at depths < 50 km (i.e. shallower than the top of the low K/Nb distribution and shallower than the top of the melting column estimated from REE inverse modeling). Their distribution is more consistent with the effects of conductive cooling at the base of the lithosphere. This observation is also consistent with our interpretation that enrichment derives from the melting of, or contamination by, an enriched lithosphere.

It is conceivable that geographical variations in source composition and oxidation state could influence the robustness of the observed gradient in T_P across Anatolia. Although source composition is allowed to vary regionally for REE inverse modeling, we have kept all other parameters in our analyses fixed. Reconciling the estimated temperature differences would require more extreme variations in these parameters. Given similarities in isotopic and elemental compositions for high-Mg samples from the region, such large variations are less likely. We conclude that the estimated temperature gradient is a robust reflection of the asthenospheric temperature pattern beneath Anatolia.

In their study of the Hasan basalts from Central Anatolia, *Reid et al.* [2017] also estimated mantle potential temperatures using the *Plank and Forsyth* [2016] thermobarometer. They conclude that melt equilibration beneath the Hasan field was significantly shallower and colder than to the west and east. Analysis of our more comprehensive database reproduces this result. However, the majority of Hasan samples have K/Nb values that exceed 500 which places them within the enriched population identified above. Elevated potential temperatures are estimated for unenriched samples from the nearby Sivas and Erciyes lava fields. We infer that the Hasan basalts are not necessarily representative of asthenospheric melting beneath Central Anatolia. Instead, our results imply that asthenospheric temperatures beneath Central Anatolia are indeed anomalously elevated.

Reid et al. [2017] also report elevated temperatures across Western and Eastern Anatolia. For Eastern Anatolia, their maximum temperature estimates range from 1380 to 1430 ° C, in broad agreement with our results. Notably, they do not recover a westward temperature decrease. Instead, their maximum temperature estimates of ~ 1450 ° C occur in Western Anatolia where our estimates are much closer to those of ambient mantle. Minor disparities in melt equilibration estimates can arise due to differences in chosen parameters. Significantly, *Reid et al.* [2017] chose to correct for the effects of latent heat by employing the scheme described by *Putirka et al.* [2007]. This scheme relies on an estimate of melt fraction that carries a large degree of uncertainty. Thus high melt fraction estimates of ~10% for Western Anatolia require a significant latent heat correction (i.e. ~ +70 °C). Our procedure of fitting melting paths through suites of melt equilibration estimates combined with REE inverse modeling yields much lower estimates of melt frac-

tion for Western Anatolia (i.e. ~ 4 and ~ 2 %, respectively), and thus cooler temperatures. Applying the latent heat correction of *Putirka et al.* [2007] to these lower melt fraction estimates would also result in significantly cooler calculated temperatures, accounting for most of the difference between our results and those of *Reid et al.* [2017]. In summary, we believe that a wealth of disparate evidence supports the presence of a westward decrease in asthenospheric potential temperature across Anatolia.

5 Constraints from Tomographic Models

Earthquake tomographic models provide a useful independent constraint on the thermal structure of the sub-plate mantle because seismic wave speeds, especially those of shear waves, are strongly dependent on temperature. Several studies have built tomographic models of the mantle beneath Anatolia using a range of datasets and techniques [e.g. *Bakırcı et al.*, 2012; *Salaün et al.*, 2012; *Chamorro et al.*, 2014; *Skolbeltsyn et al.*, 2014; *Govers and Fichtner*, 2016]. In Figure 16, we summarize results from two studies: a regional *P*-wave model [*Biryol et al.*, 2011]; and part of a global upper mantle shear wave model [*Priestley and McKenzie*, 2013]. Both models suggest that mantle material that lies immediately beneath the lithospheric plate (i.e. shallower than ~ 250 km) is anomalously slow. The relative sizes of these anomalies are largest beneath Eastern Anatolia and decrease westward. Beneath a depth of 250 km, a continuous fast anomaly extends across most of Anatolia, which is interpreted as subducted African lithosphere. This anomaly is clearest in the *P*-wave model, which is particularly sensitive to cold temperatures.

Yamauchi and Takei [2016] present a parameterization that enables shear wave velocities to be converted into temperature. Their approach builds upon the earlier work of *Priestley and McKenzie* [2013]. Here, we apply this revised parameterization to the upper mantle shear wave model of *Priestley and McKenzie* [2013]. The eastward decrease in shear wave velocity is reflected in the resulting T_P model (Figure 17a,b). Note that at depths shallower than 100 km, tomographic models are likely to be affected by artefacts related to uncertainties in crustal structure [*Priestley and McKenzie*, 2013]. Beneath 100 km, a long wavelength high temperature feature is recovered beneath Eastern Anatolia, extending to depths of ~ 200 km and with asthenospheric potential temperatures up to ~ 1400 °C. The magnitude and extent of this high temperature feature decrease westward.

In Figure 17c, average potential temperatures between depths of 100 and 200 km that have been calculated from the shear wave velocity model are compared with temperatures obtained by both petrologic approaches. T_P estimates for each region are calculated by averaging T_P estimates at locations with petrological constraints. Although uncertainties in seismologic T_P are quoted in terms of standard deviations of mean values, we must emphasise that larger, but less easily quantifiable, uncertainties are associated with the tomographic model and with the temperature parametrization. There is a reasonable correlation between potential temperatures estimated using petrological and seismological approaches. This agreement strengthens the notion that sub-plate mantle temperatures are highest beneath Eastern Anatolia and decrease westward.

6 Discussion

We have exploited a range of diverse approaches to investigate the causes of Neogene uplift and magmatism across Anatolia. A compilation of published receiver function analyses is used to investigate the isostatic relationship between crustal thickness and elevation for different lithospheric thicknesses and densities. One plausible interpretation is that post-Miocene regional uplift of 1–2 km is generated by some combination of lithospheric thinning/loss of ~ 75–125 km and/or asthenospheric temperature anomalies. Admittance analysis of topographic and gravity datasets indicates that, at the longest wavelengths, Anatolian topography is not supported by flexural isostasy.

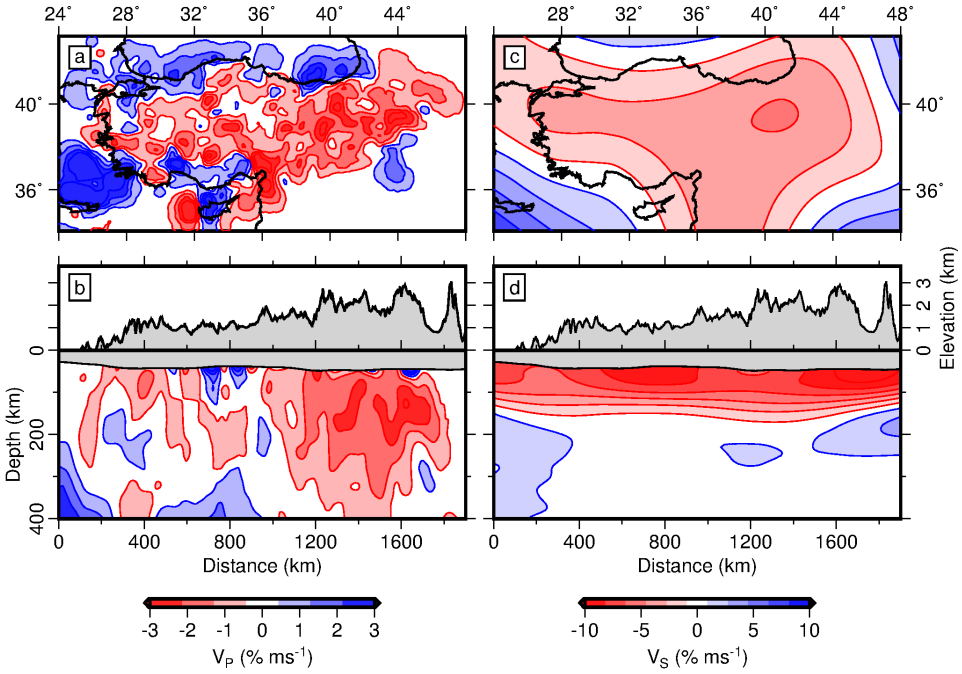

Figure 16. (a) Regional earthquake tomographic model of Anatolia based upon *P*-wave arrivals [*Biryol et al.*, 2011]. (b) East-west vertical slice at 39°N through model shown in panel (a). Black line with gray band = topographic and crustal thickness profile from EPcrust reference model of *Molinari and Morelli* [2011]. (c) Surface wave tomographic model [*Priestley and McKenzie*, 2013]. (d) East-west vertical slice.

Marine sedimentary rocks of Miocene age that are patchily distributed across Anatolia suggest that significant uplift has occurred in Neogene times. Longitudinal river profiles that drain the Central and East Anatolian Plateaux contain prominent knickzones that indirectly record this phase of regional uplift. Calibrated inverse modeling of these profiles suggests that uplift began at about 20 Ma in Eastern Anatolia and subsequently propagated westward. Uplift rates across Anatolia increased throughout Neogene times to reach peak values of 0.2–0.4 mm yr^{-1}, coinciding with the onset of OIB-style magmatism. Modeling of the geochemistry of these basalts indicates that asthenospheric temperatures vary across the region: the highest estimates of up to 1400°C are for Eastern Anatolia, decreasing toward Western Anatolia. These modeling results also imply that lithospheric thickness is ~ 60 km beneath volcanic regions. It is unclear whether this such low lithospheric thicknesses occur throughout Anatolia. Our results have significant implications for the the geodynamical evolution of this region.

Occurrence of a Miocene transition from calc-alkaline to alkaline magmatism within Western Anatolia is well established. Recently, several authors have linked this transition to the opening of a 'slab window' within the subducting African lithosphere [*Innocenti et al.*, 2005; *Agostini et al.*, 2007; *Klaver et al.*, 2016]. Such a window is purported to have been imaged in several tomographic models [*Biryol et al.*, 2011; *Govers and Fichtner*, 2016]. Geochemical analyses confirm a clear shift from arc to intraplate-style magmatism, culminating at about 10 Ma. After this time, basaltic compositions are similar to those derived from an unenriched mantle source. Major element thermobarometric calculations and inverse modeling of REEs suggest low degree decompression melting at approximately ambient mantle temperatures. Both sets of observations are consistent with passive upwelling of sub-slab asthenospheric mantle, possibly in response to slab fragmentation.

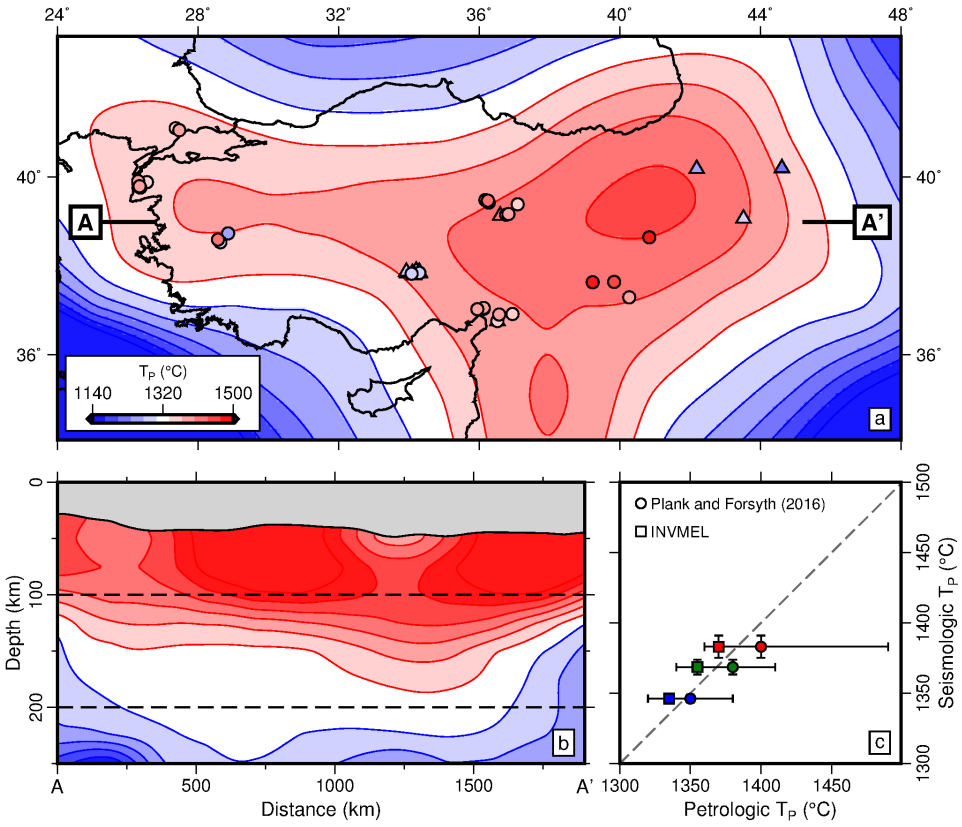

Figure 17. (a) Map of Anatolia showing potential temperatures calculated from shear wave velocity model of *Priestley and McKenzie* [2013] using parametrization of *Yamauchi and Takei* [2016]. Circles/triangles = potential temperature estimates determined from major element thermobarometry for individual basaltic samples with K/Nb < 500 and > 500, respectively. (b) Vertical slice through potential temperature model. Pair of dashed lines = depth range over which average T_P was estimated. (c) Relationship between estimates of potential temperature from geochemical and seismological techniques. Blue/green/red squares and circles = potential temperature estimates for Western/Central/Eastern Anatolia from inverse modeling of REE concentrations and major element thermobarometry, respectively [*McKenzie and O'Nions*, 1991; *Plank and Forsyth*, 2016].

Further east, there is little evidence for subduction-driven magmatism. Rather, for Central Anatolia, magmas with intraplate to mildly enriched compositions were produced during two distinct Neogene phases. Magmatic rocks with similar compositions occur in Eastern Anatolia after ~ 10 Ma. Thermobarometric estimates of melting conditions indicate that partially enriched magmas equilibrated at cool temperatures and at depths within the lithospheric mantle. In contrast, magmas with K/Nb ratios of less than 500 have equilibrated at greater depths and require elevated asthenospheric temperatures. As noted previously, onset of more recent phases of magmatism in both Central and Eastern Anatolia post-date initiation of regional uplift by ~ 10 Ma. These results suggest that mantle underlying Central and particularly Eastern Anatolia is anomalously hot with a composition similar to that of OIB source reservoirs.

Consistent patterns linking onset of uplift and magmatism together with the magnitude of uplift and size of temperature excess all point toward a common cause. In Eastern Anatolia, several authors invoke slab break-off following collision of Arabia and Eurasia [*Keskin*, 2003; *Şengör et al.*, 2003; *Neill et al.*, 2015; *Lebedev et al.*, 2016a]. Detachment of subducting African lithosphere at ~ 10 Ma has also been proposed. This suggestion is based on the observed transition from subduction-related (i.e. calc-alkaline) to intraplate-style magmatism for low MgO basaltic rocks [e.g. *Keskin*, 2003, 2007; *Faccenna et al.*, 2014]. However, there is little evidence for this transition in the database of high-Mg basaltic rocks. Nonetheless, this detachment model is supported by observations of a continuous high velocity anomaly at transition zone depths beneath Anatolia, interpreted as remnant subducted lithosphere [Figure 16; e.g. *Biryol et al.*, 2011]. Therefore, while slab break-off has probably occurred, its timing and nature are not well constrained by the geochemistry of Neogene basaltic magmas. Several authors have also suggested that removal of Anatolian lithosphere could drive uplift and magmatism [*Göğüş and Pysklywec*, 2008; *Bartol and Govers*, 2014]. In this case, uplift and magmatism are thought to have been caused by upwelling of buoyant asthenospheric mantle, triggered in turn by removal of dense lithospheric material. However, this mechanism alone will not generate elevated asthenospheric temperatures. We suggest that the effects of slab detachment and/or delamination are enhanced and magnified by replacement of lithospheric material with anomalously hot asthenospheric mantle. Indeed, a range of laboratory and numerical experiments suggest that asthenospheric thermal anomalies may drive significant loss of lithospheric material by thermal erosion [e.g. *Olsen et al.*, 1988; *Davies*, 1994].

Following onset of uplift in Eastern Anatolia, uplift propagated westward, commencing across Central Anatolia by about 15 Ma. It has been proposed that delamination of the Cyprean slab, following a period of flat subduction, might account for observed uplift and magmatism across Central Anatolia [*Bartol and Govers*, 2014; *Govers and Fichtner*, 2016]. Magmatism in the vicinity of Sivas and Erciyes requires elevated mantle potential temperatures, similar to observations from Eastern Anatolia. Our modeled results are consistent with lateral propagation of hot asthenospheric material from Eastern to Central Anatolia. Such an interpretation is supported by seismic tomographic images that reveal a continuous low velocity anomaly beneath Eastern and Central Anatolia [Figure 16; **?**].

Along the southern edge of the Central Anatolian Plateau, emergent marine sedimentary rocks and disequilibrated river profiles both attest to elevated regional uplift rates during the last 10 Ma [*Schildgen et al.*, 2014]. This area overlies a 'slab tear' identified by *Biryol et al.* [2011]. The nearby Hasan volcanic field is anomalous since the composition of its basalts suggests that melting is occurring at shallow depths with cool temperatures, possibly reflecting a combination of conductive cooling and contamination at the base of the lithosphere. Numerical modeling indicates that uplift rates of 0.1 to 0.8 mm yr^{-1} and extension of the overriding plate can occur following break-off of subducting slabs, consistent with regional uplift histories we obtain from linear inverse modeling of drainage networks [*Duretz et al.*, 2011; *van Hunen and Allen*, 2011]. It is therefore conceivable that opening of a slab window is driving additional uplift due to uncoupling of the slab

and additional melting caused by subsequent lithospheric stretching with passive asthenospheric upwelling.

What is the cause of the elevated asthenospheric temperatures inferred beneath Central and Eastern Anatolia? Recent global studies of oceanic residual depths and their correlation with a range of geophysical and geologic observations suggest that significant thermal anomalies are a common feature of the sub-plate asthenosphere [*Hoggard et al.*, 2016, 2017]. *Faccenna et al.* [2013] invoke material upwelling beneath Afar and spreading laterally beneath Arabia and Anatolia to explain a range of regional observations. *Wilson et al.* [2014] analyze drainage networks and patterns of basaltic magmatism in Arabia, and describe a northward progression of uplift and magmatism throughout Cenozoic times consistent with the movement of asthenospheric thermal anomalies. Lateral displacement of hot plume material from beneath Afar would therefore appear to be a plausible mechanism for generating elevated asthenospheric temperatures beneath Anatolia.

It is likely that growth of Anatolian plateaux has exerted a profound influence on its tectonic evolution. Several recent studies have suggested that mantle flow drives lithospheric deformation, by exerting tractions on the base of the lithosphere [*Faccenna and Becker*, 2010; *Faccenna et al.*, 2013]. However, *England et al.* [2016] suggest that much of the observed modern crustal deformation could instead be generated by gradients in gravitational potential energy. They argue that the juxtaposition of elevated topography across the East Anatolian Plateau and depressed bathymetry south of the Hellenic trench drives westward motion of crustal material. Figure 18 shows residual depth measurements, temperature estimates, and inferred dynamic topography estimated from long wavelength free-air gravity anomalies using an admittance value of $Z = 30$ mGal km^{-1} [*Hoggard et al.*, 2017]. In the Eastern Mediterranean Sea, there is a substantial negative residual depth anomaly, which we interpret as dynamic drawdown of 1–2 km. The Black Sea is similarly drawn down with evidence for an east-west gradient. Anatolia itself is a westward-protruding finger of continental lithosphere, which is characterized by inferred dynamic uplift of 1–2 km, probably supported by a combination of thin lithosphere and elevated asthenospheric potential temperatures that decrease from east to west. Finally, the fluvial drainage network is radially draped around positive long wavelength gravity anomalies. Thus it appears that mantle convective processes produce the dramatic gradients of gravitational potential energy that modulate lithospheric deformation without the requirement for significant tractions along the base of the lithospheric plate.

7 Conclusions

We have combined geomorphic and geochemical observations to investigate the geodynamic evolution of Anatolia. Analysis of Anatolian drainage networks provides additional insights into the spatial and temporal evolution of regional epeirogeny. The bulk of Anatolia became emergent in Neogene times when regional uplift initiated in the east and propagated westward. This uplift pattern cannot be explained by the geometry of active deformation, by crustal thickness variations, or by flexural processes. Basaltic magmatism that occurred over the last 10 Ma is of OIB affinity and requires melting of anomalously hot asthenospheric mantle beneath the high plateaux.

Slab detachment/fragmentation and lithospheric delamination are often invoked to account for Neogene uplift and magmatism across Anatolia. Our results suggest that asthenospheric thermal anomalies play a significant role in generating regional uplift and basaltic magmatism. Quantitative estimates of regional uplift rates and asthenospheric temperatures should provide useful constraints for numerical simulations of Anatolia's geodynamic evolution.

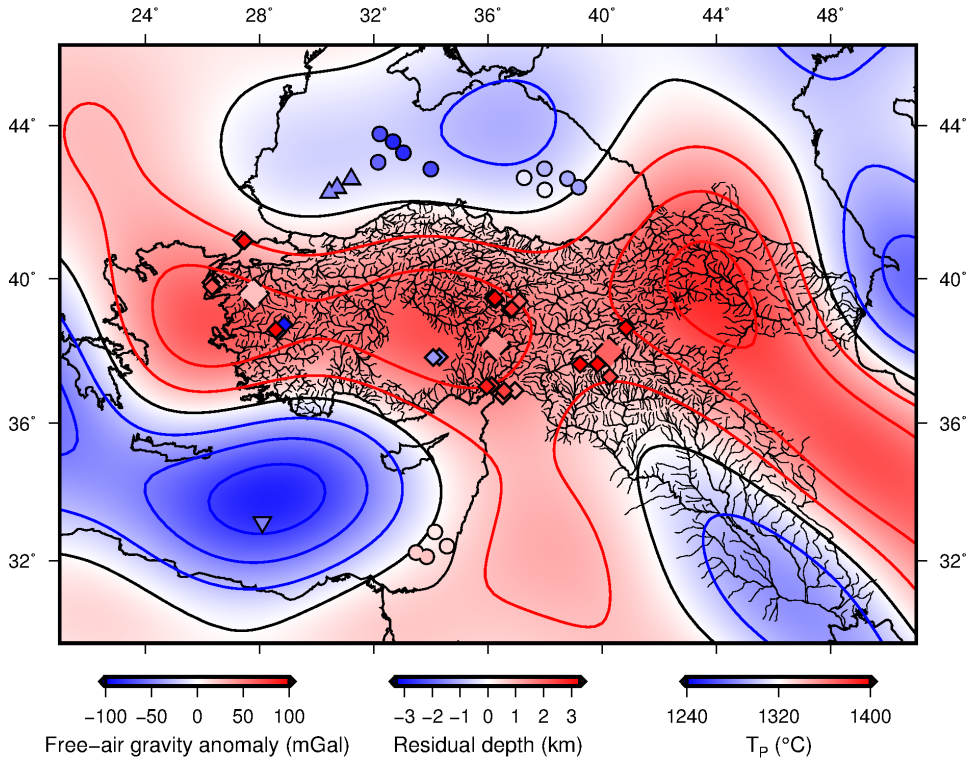

Figure 18. Map of region encompassing Anatolia showing long wavelength (i.e. 730 – 13,000 km) free-air gravity anomalies. Red/black/blue contours = positive/zero/negative GGM03C anomalies plotted every 25 mGal [*Tapley et al.*, 2007]; residual depth scale assumes Z = 30 mGal km^{-1}; colored circles and upward/downward-pointing triangles = estimates and lower/upper bounds of observed oceanic residual depths [*Hoggard et al.*, 2017]; colored big/small diamonds = potential temperature estimates from forward/inverse modeling of major and rare earth elements, respectively (note that big dashed diamonds represent average values for Eastern/Central/Western Anatolia); irregular network of black lines = river drainage pattern.

Acknowledgments

This project is supported by Shell Research. We thank G. L. Farmer, T. Plank and an anonymous reviewer for their careful and constructive comments. We are grateful to B. Biryol, L. Cowton, I. Frame, L. Kennan, M. Klöcking, D. Lyness, J. Mclennan, F. Richards, S. Shorttle, S. Stephenson and D. Smit for their help. D. McKenzie generously provided software for calculating admittance and REE concentrations. All data used are publicly available, either via the references cited or in Data Sets S1-3 (Supporting Information and in the University of Cambridge online repository, doi.org/10.17863/CAM.17105). Department of Earth Sciences contribution number esc.4081.

References

Adiyaman, O., J. Chorowicz, O. N. Arnaud, M. N. Gündogdu, and A. Gourgaud (2001), Late Cenozoic tectonics and volcanism along the North Anatolian Fault: new structural and geochemical data, *Tectonophysics*, *338*, 135–165.

Agostini, S., C. Doglioni, F. Innocenti, P. Manetti, S. Tonarini, and M. Savasçin (2007), The transition from subduction-related to intraplate Neogene magmatism in the Western Anatolia and Aegean area, in *Cenzozoic volcanism in the Mediterranean Area*, edited by L. Beccaluva, G. Bianchini, and M. Wilson, pp. 1–15, The Geological Society of America, Boulder, Colorado, doi:10.1130/2007.2418(01)., geological Society of America Special Paper 418.

Akbayram, K., C. C. Sorlien, and A. I. Okay (2016), Evidence for a minimum 52 ± 1 km of total offset along the northern branch of the North Anatolian Fault in northwest Turkey, *Tectonophysics*, *668–669*, 35–41, doi:10.1016/j.tecto.2015.11.026.

Aktuğ, B., E. Parmaksiz, M. Kurt, O. Lenk, A. Kiliçoğlu, M. Ali Gürdal, and S. Özdemir (2013), Deformation of central anatolia: GPS implications, *Journal of Geodynamics*, *67*, 78–96, doi:10.1016/j.jog.2012.05.008.

Aktuğ, B., J. M. Nocquet, A. Cingöz, B. Parsons, Y. Erkan, P. England, O. Lenk, M. A. Gürdal, A. Kilicoglu, H. Akdeniz, and A. Tekgül (2009), Deformation of western Turkey from a combination of permanent and campaign GPS data: Limits to block-like behavior, *Journal of Geophysical Research: Solid Earth*, *114*(10), 1–22, doi: 10.1029/2008JB006000.

Aldanmaz, E., J. A. Pearce, M. F. Thirwall, and J. G. Mitchell (2000), Petrogenetic evolution of late Cenozoic, post-collision volcanism in western Anatolia, Turkey, *Journal of Volcanology and Geothermal Research*, *102*, 67–95.

Aldanmaz, E., Köprübaşı, O. F. Gürer, N. Kaymakçı, and A. Gourgaud (2006), Geochemical constraints on the Cenozoic, OIB-type alkaline volcanic rocks of NW Turkey: Implications for mantle sources and melting processes, *Lithos*, *86*, 50–76, doi: 10.1016/j.lithos.2005.04.003.

Aldanmaz, E., M. Pickard, T. Meisel, c. Altunkaynak, K. Sayıt, P. Şen, B. B. Hanan, and T. Furman (2015), Source components and magmatic processes in the genesis of Miocene to Quaternary lavas in western Turkey: constraints from HSE distribution and Hf-Pb-Os isotopes, *Contributions to Mineral Petrology*, *170*, 23, doi:10.1007/s00410-015-1176-x.

Alıcı, P., A. Temel, A. Gourgaud, P. Vidal, and M. N. Gündogdu (2001), Quaternary tholeiitic to alkaline volcanism in the Karasu Valley, Dead Sea Rift Zone, Southeast Turkey: Sr-Nd-Pb-O isotopic and trace-element approached to crust-mantle interaction, *International Geology Review*, *43*, 120–138.

Alıcı, P., A. Temel, and A. Gourgaud (2002), Pb-Nd-Sr isotope and trace element geochemistry of Quaternary extension-related alkaline volcanism: a case study of Kula region (western Anatolia, Turkey), *Journal of Volcanology and Geothermal Research*, *115*, 487–510.

Alıcı Şen, P., A. Temel, and A. Gourgaud (2004), Petrogenetic modelling of Quaternary post-collisional volcanism: a case study of central and eastern Anatolia, *Geological*

Magazine, *141*(1), 81–98, doi:10.1017/S0016756803008550.

Alpaslan, M. (2007), Early to middle Miocene intra-continental basaltic volcanism in the northern part of the Arabian plate, SE Anatolia, Turkey: geochemistry and petrogenesis, *Geological Magazine*, *144*(5), 867–882, doi:10.1017/S001675680700352.

Angus, D. A., D. C. Wilson, E. Sandvol, and J. F. Ni (2015), Lithospheric structure of the Arabian and Eurasian collision zone in eastern Turkey from *S*-wave receiver functions, *Geophysical Journal International*, *166*, 1335–1346, doi:10.1111/j.1365-246X.2006.03070.x.

Arger, J., J. Mitchell, and R. W. C. Westaway (2000), Neogene and Quaternary volcanism of southeastern Turkey, in *Tectonics and Magmatism in Turkey and the Surrounding Area*, edited by E. Bozkurt, W. J. A., and J. D. A. Piper, pp. 459–487, The Geological Society of London, London, Special Publications 173.

Asan, K., and H. Kurt (2011), Petrology and geochemistry of post-collisional Early Miocene volcanism in the Karacadağ area (Central Anatolia, Turkey), *Acta Geologica Sinica*, *85*(5), 1100–1117.

Aslan, Z., M. Arslan, I. Temizel, and A. Kaygusuz (2014), K-Ar dating, whole-rock and Sr-Nd isotope geochemistry of calc-alkaline volcanic rocks around the Gümüşhane area: implications for post-collisional volcanism in the Eastern Pontides, Northeast Turkey, *Mineral Petrology*, *108*, 245–267, doi:10.1007/s00710-013-0294-2.

Audet, P. (2014), Toward mapping the effective elastic thickness of planetary lithospheres from a spherical wavelet analysis of gravity and topography, *Physics of the Earth and Planetary Interiors*, *226*, 48–82, doi:10.1016/j.pepi.2013.09.011.

Aydin, F., O. Karsli, and B. Chen (2008), Petrogenesis of the Neogene alkaline volcanics with implications for post-collisional lithospheric thinning of the Eastern Pontides, NE Turkey, *Lithos*, *104*, 249–266, doi:10.1016/j.lithos.2007.12.010.

Bakırcı, T., K. Yoshizawa, and M. F. Özer (2012), Three-dimensional *S*-wave structure of the upper mantle beneath Turkey from surface wave tomography, *Geophysical Journal International*, *190*, 1058–1076, doi:j.1365-246X.2012.05526.x.

Ballato, P., C. E. Uba, A. Landgraf, M. R. Strecker, M. Sudo, D. F. Stockli, A. Friedrich, and S. H. Tabatabaei (2011), Arabia-Eurasia continental collision: Insights from late Tertiary foreland-basin evolution in the Alborz Mountains, Northern Iran, *Bulletin of the Geological Society of America*, *123*(1-2), 106–131, doi:10.1130/B30091.1.

Bartol, J., and R. Govers (2014), A single cause for uplift of the Central and Eastern Anatolian plateau?, *Tectonophysics*, *637*, 116–136, doi:10.1016/j.tecto.2014.10.002.

Bebout, G. E. (2007), Metamorphic chemical geodynamics of subduction zones, *Earth and Planetary Science Letters*, *260*, 373–393, doi:10.1016/j.epsl.2007.05.050.

Becker, J., D. Sandwell, W. Smith, J. Braud, B. Binder, J. Depner, F. D., J. Factor, S. Ingalls, S.-H. Kim, R. Ladner, K. Marks, S. Nelson, A. Pharoah, R. Trimmer, J. von Rosenberg, G. Wallace, and P. Weatherall (2009), Global bathymetry and elevation data at 30 arc second resolution: SRTM30_plus, *Marine Geology*, *32*(4), 355–371.

Biryol, C. B., S. L. Beck, G. Zandt, and A. A. Özacar (2011), Segmented African lithosphere beneath the Anatolian region inferred from teleseismic P-wave tomography, *Geophysical Journal International*, *184*(3), 1037–1057, doi:10.1111/j.1365-246X.2010.04910.x.

Blundy, J., and B. Wood (2003), Partitioning of trace elements between crystals and melts, *Earth and Planetary Science Letters*, *210*, 383–397, doi:10.1016/S0012-821X(03)00129-8.

Boschi, L., C. Faccenna, and T. W. Becker (2010), Mantle structure and dynamic topography in the Mediterranean Basin, *Geophysical Research Letters*, *37*, L20,303, doi:10.1029/2010GL045001.

Bozkurt, E., J. A. Winchester, G. Ruffet, and B. Rojay (2008), Age and chemistry of Miocene volcanic rocks from the Kiraz Basin of the Küçük Menderes Graben: Its significance for the extensionsional tectonics of Southwestern Anatolia, Turkey, *Geodinamica Acta*, *21*(5–6), 239–257, doi:0.3166/ga.21.239-257.

Brounce, M. N., K. A. Kelley, and E. Cottrell (2014), Variations in $Fe^{3+}/\Sigma Fe$ of Mariana Arc basalts and mantle wedge fO_2, *Journal of Petrology*, *55*(12), 2513–2536, doi:10.1093/petrology/egu065.

Çakır, O., and M. Erduran (2004), Constraining crustal and uppermost mantle structure beneath station TBZ (Trabzon, Turkey) by receiver function and dispersion analyses, *Geophysical Journal International*, *158*, 955–971, doi:10.1111/j.1365-246X.2004.02345.x.

Çakır, O., and M. Erduran (2011), On the *P* and *S* receiver functions used for inverting the one-dimensional upper mantle shear-wave velocities, *Surveys in Geophysics*, *32*, 71–98, doi:10.1007/s10712-010-9108-9.

Çiner, A., E. Kosun, and M. Deynoux (2002), Fluvial, evaporitic and shallow-marine facies architecture, depositional evolution and cyclicity in the Sivas Basin (Lower to Middle Miocene), Central Turkey, *Journal of Asian Earth Sciences*, *21*, 147–165.

Chamorro, C. R., J. L. Garcia-Cuesta, M. E. Mondéjar, and A. Pérez-Madrazo (2014), Enhanced geothermal systems in Europe: An estimation and comparison of the technical and sustainable potentials, *Energy*, *65*, 250–263, doi:10.1016/j.energy.2013.11.078.

Cipollari, P., D. Cosentino, G. Radeff, T. F. Schildgen, C. Faranda, F. Grossi, E. Gliozzi, A. Smedile, R. Gennari, G. Darbaş, F. Ö. Dudas, K. Gürbüz, A. Nazik, and H. Echtler (2012), Easternmost Mediterranean evidence of the Zanclean flooding event and subsequent surface uplift: Adana Basin, southern Turkey, *Geological Society, London, Special Publications*, *372*(1), 473–494, doi:10.1144/sp372.5.

Cipollari, P., E. Halásová, K. Gürbüz, and D. Cosentino (2013), Middle-Upper Miocene paleogeography of southern Turkey: Insights from stratigraphy and calcareous nannofossil biochronology of the Olukpi{dotless}nar and Başyayla sections (Mut-Ermenek Basin), *Turkish Journal of Earth Sciences*, *22*(5), 820–838, doi:10.3906/yer-1208-2.

Çoban, H. (2007), Basalt magma genesis and fractionation in collision- and extension-related provinces: A comparison between eastern, central and western Anatolia, *Earth-Science Reviews*, *80*(3-4), 219–238, doi:10.1016/j.earscirev.2006.08.006.

Colli, L., S. Ghelichkhan, and H.-P. Bunge (2016), On the ratio of dynamic topography and gravity anomalies in a dynamic Earth, *Geophysical Research Letters*, *43*(6), 2510–2516, doi:10.1002/2016GL067929.

Cosentino, D., T. F. Schildgen, P. Cipollari, C. Faranda, E. Gliozzi, N. Hudákovčá, S. Lucifora, and M. R. Strecker (2012), Late Miocene surface uplift of the southern margin of the Central Anatolian plateau, Central Taurides, Turkey, *Bulletin of the Geological Society of America*, *124*(1-2), 133–145, doi:10.1130/B30466.1.

Cottrell, E., and K. A. Kelley (2011), The oxidation state of Fe in MORB glasses and the oxygen fugacity of the upper mantle, *Earth and Planetary Science Letters*, *305*, 270–282, doi:10.1016/j.epsl.2011.03.014.

Crosby, A. G., S. Fishwick, and N. White (2010), Structure and evolution of the intracratonic Congo Basin, *Geochemistry, Geophysics, Geosystems*, *11*(6), Q06,010, doi:10.1029/2009GC003014.

Czarnota, K., G. Roberts, N. White, and S. Fishwick (2014), Spatial and temporal patterns of Australian dynamic topography from river profile modeling, *Journal of Geophysical Research: Solid Earth*, *119*, 1384–1424, doi:10.1002/2013JB010436.

Dalton, C. A., C. H. Langmuir, and A. Gale (2014), Geophysical and geochemical evidence for deep temperature variations beneath mid-ocean ridges, *Science*, *344*(6179), 80–83, doi:10.1126/science.1249466.

Davies, G. F. (1994), Thermochemical erosion of the lithosphere by mantle plumes, *Journal of Geophysical Research*, *99*(B8), 15,709–15,722.

Demir, T., R. Westaway, D. Bridgland, M. Pringle, S. Yurtmen, A. Beck, and G. Rowbotham (2007), Ar-Ar dating of late Cenozoic basaltic volcanism in northern Syria: Implications for the history of incision by the River Euphrates and uplift of the northern Arabian Platform, *Tectonics*, *26*, TC3012, doi:doi:10.1029/2006TC001959.

Demir, T., A. Seyrek, R. Westaway, H. Guillou, S. Scaillet, A. Beck, and D. R. Bridgland (2012), Late Cenozoic regional uplift and localised crustal deformation within the northern Arabian Platform in southeast Turkey: Investigation of the Euphrates terrace staircase using multidisciplinary techniques, *Geomorphology*, *165–166*, 7–24, doi: 10.1016/j.geomorph.2012.01.005.

DePaulo, D. J. (1981), Trace element and isotopic effects of combined wallrock assimilation and fractional crystallization, *Earth and Planetary Science Letters*, *53*, 189–202.

Dixon, J. E., L. Leist, C. Langmuir, and J.-G. Schilling (2002), Recycled dehydrated lithosphere observed in plume-influenced mid-ocean-ridge basalt, *Nature*, *420*, 385–389, doi: 10.1038/nature01215.

Duretz, T., T. V. Gerya, and D. A. May (2011), Numerical modelling of spontaneous slab breakoff and subsequent topographic response, *Tectonophysics*, *502*, 244–246, doi: 10.1016/j.tecto.2010.05.024.

Dziewonski, A. M., T. A. Chou, and J. H. Woodhouse (1981), Determination of earthquake source parameters from waveform data for studies of global and regional seismicity, *Journal of Geophysical Research*, *86*(B4), 2825–2852, doi:10.1029/JB086iB042825.

Ekici, T., M. Alpaslan, O. Parlak, and A. Uçurum (2009), Geochemistry of the middle Miocene collision-related Yamadağı (Eastern Anatolia) calc-alkaline volcanics, Turkey, *Turkish Journal of Earth Science*, *18*, 511–528, doi:10.3906/yer-0712-1.

Ekström, G., M. Nettles, and A. M. Dziewonski (2012), The global CMT project 2004–2010: centroid moment tensors for 13,017 earthquakes, *Physics of the Earth and Planetary Interiors*, *200–201*, 1–9, doi:10.1016/j.pepi.2012.04.002.

Elliott, T. (2003), Tracers in the Slab, in *Inside the Subduction Factory*, edited by J. Eiler, pp. 23–45, American Geophysical Union, Washington D.C., doi:10.1029/GM138, gephysical Monograph 138.

England, P., G. Houseman, and J. M. Nocquet (2016), Constraints from GPS measurements on the dynamics of deformation in Anatolia and the Aegean, *Journal of Geophysical Research: Solid Earth*, *121*(12), 8888–8916, doi:10.1002/2016JB013382.

Erduran, M. (2009), Teleseismic inversion of crustal *S*-wave velocities beneath Isparta station, *Journal of Geodynamics*, *47*, 225–236, doi:10.1016/j.jog.2008.10.001.

Erkül, F., C. Helvacı, and H. Sözbilir (2005), Evidence for two episodes of volcanism in the Bigadiç borate basin and tectonic implications for western Turkey, *Geological Journal*, *40*, 545–570, doi:10.1002/gj.1026.

Ersoy, E. Y., C. Helvacı, and M. R. Palmer (2010), Mantle source characteristics and melting models for the early-middle Miocene mafic volcanism in Western Anatolia: Implications for enrichment processes of mantle lithosphere and origin of K-rich volcanism in post-collisional settings, *Journal of Volcanology and Geothermal Research*, *198*, 112–128, doi:10.1016/j.jvolgeores.2010.08.014.

Ersoy, Y., C. Helvacı, H. Sözbilir, F. Erkül, and E. Bozkurt (2008), A geochemical approach to Neogen-Quaternary volcanic activity of western Anatolia: An example of episodic bimodal volcanism within the Selendi Basin, Turkey, *Chemical Geology*, *255*, 265–282, doi:10.1016/j.chemgeo.2008.06.044.

Ersoy, Y. E., C. Helvacı, and M. R. Palmer (2012), Petrogenesis of the Neogene volcanic unist in the NE–SW-trending basins in western Anatolia, Turkey, *Contributions to Mineral Petrology*, *163*, 379–401, doi:10.1007/s00410-011-0679-3.

Ersoy, Y. E., M. R. Palmer, I. Uysal, and I. Gündoğan (2014), Geochemistry and petrology of the Early Miocene lamproites and related volcanic rocks in the Thrace Basin, NW Anatolia, *Journal of Volcanology and Geothermal Research*, *283*, 143–158, doi: 10.1016/j.jvolgeores.2014.06.016.

Faccenna, C., and T. Becker (2010), Shaping mobile belts by small-scale convection, *Nature*, *465*, 602–605, doi:10.1038/nature09064.

Faccenna, C., T. W. Becker, L. Jolivet, and M. Keskin (2013), Mantle convection in the Middle East: Reconciling Afar upwelling, Arabia indentation and Aegean trench rollback, *Earth and Planetary Science Letters*, *375*, 254–269, doi:

10.1016/j.epsl.2013.05.043.

Faccenna, C., T. W. Becker, L. Auer, A. Billi, L. Boschi, J. P. Brun, F. A. Capitanio, F. Funiciello, F. Horvàth, L. Jolivet, C. Piromallo, L. Royden, F. Rossetti, and E. Serpelloni (2014), Mantle dynamics in the Mediterranean, *Reviews of Geophysics*, *52*, 283–332, doi:10.1002/2013RG000444.

Fitton, J. G., D. James, and W. P. Leeman (1991), Basic magmatism associated with Late Cenozoic extension in the Western United States: compositional variations in space and time, *Journal of Geophysical Research*, *96*(B8), 13,693–17,711.

Förste, C., S. L. Bruinsma, F. Flechtner, J.-C. Marty, J.-M. Lemoine, C. Dahle, O. Abrikosov, K. H. Neumayer, R. Biancale, F. Barthelmes, and G. Balmino (2012), A preliminary update of the Direct approach GOCE Processing and a new release of EIGEN-6C, in *AGU Fall Meeting*, San Francisco, USA.

Fox, M., L. Goren, D. A. May, and S. D. Willett (2014), Inversion of fluvial channels for paleorock uplift rates in Taiwan, *Journal of Geophysical Research: Earth Surface*, *119*, 1853–1875, doi:10.1002/2014JF003196.

Gencalioglu-Kuscu, G. (2011), Geochemical characterization of a Quaternary monogenetic volcano in Erciyes Volcanic Complex: Cora Maar (Central Anatolian Volcanic Province, Turkey), *International Journal of Earth Sciences*, *100*, 1967–1985, doi:10.1007/s00531-010-0620-4.

Gencalioglu-Kuscu, G., and F. Geneli (2010), Review of post-collisional volcanism in the Central Anatolian Volcanic Province (Turkey), with special reference to the Tepekoy Volcanic Complex, *International Journal of Earth Sciences*, *99*, 593–621, doi:0.1007/s00531-008-0402-4.

Ghiorso, M. S., M. M. Hirschmann, P. W. Reiners, and V. C. I. Kress (2002), The pMELTS: A revision of MELTS for improved calculation of phase relations and major element partitioning related to partial melting of the mantle to 3 GPa, *Geochemistry, Geophysics, Geosystems*, *3*(5), 1–35, doi:10.1029/2001GC000217.

Gibson, S. A., and D. Geist (2010), Geochemical and geophysical estimates of lithospheric thickness variation beneath Galápagos, *Earth and Planetary Science Letters*, *300*(3–4), 275–286, doi:10.1016/j.epsl.2010.10.002.

Göğüş, O. H., and R. N. Psyklywec (2008), Mantle lithosphere delamination driving plateau uplift and synconvergent extension in eastern Anatolia, *Geology*, *36*(9), 723–726, doi:10.1130/G24982A.1.

Göğüş, O. H., R. N. Psyklywec, A. M. C. Şengör, and E. Gün (2017), Drip tectonics and the enigmatic uplift of the Central Anatolian Plateau, *Nature Communications*, *8*(1538), doi:10.1038/s41467-017-01611-3.

Gök, R., H. Mahdi, H. Al-Shukri, and A. J. Rodgers (2008), Crustal structure of Iraq from receiver functions and surface wave dispersion: implications for understanding the deformation history of the Arabian-Eurasian collision, *Geophysical Journal International*, *172*, 1179–1187, doi:10.1111/j.1365-246X.2007.03670.x.

Goren, L., M. Fox, and S. D. Willett (2014), Tectonics from fluvial topography using formal linear inverion: Theory and applications to the Inyo Mountains, California, *Journal of Geophysical Research: Earth Surface*, *119*, 1615–1681, doi:10.1002/2014JF003079.

Govers, R., and A. Fichtner (2016), Signature of slab fragmentation beneath Anatolia from full-waveform tomography, *Earth and Planetary Science Letters*, *450*, 10–19, doi:10.1016/j.epsl.2016.06.014.

Grützner, T., D. Prelević, and C. Akal (2013), Geochemistry and origin of ultramafic enclaves and their basanitic host rock from Kula Volcano, Turkey, *Lithos*, *180–181*, 58–73, doi:10.1016/j.lithos.2013.08.001.

Gunn, R. (1943), A quantitative evaluation of the influence of the lithosphere on the anomalies of gravity, *Journal of the Franklin Institute*, *236*, 47–65.

Gürsoy, O., Ş. Kaya, Z. Çakir, O. Tatar, and O. Canbaz (2017), Determining lateral offsets of rocks along the eastern part of the North Anatolian Fault Zone (Turkey) using spectral classification of satellite images and field measurements, *Geomatics, Natural*

Hazards and Risk, doi:10.1080/19475705.2017.1318794.

Gürsu, S. (2016), A new petrogenetic model for meta-granitic rocks in the central and southern Menderes Massif – W Turkey: Implications for Cadomian crustal evolution within the Pan-African mega-cycle, *Precambrian Research*, *275*, 450–470, doi: 10.1016/j.precamres.2016.01.025.

Hart, S. R., E. H. Hauri, L. A. Oschmann, and J. A. Whitehead (1992), Mantle Plumes and Entrainment: Isotopic Evidence, *Science*, *256*(5056), 517–520.

Helvacı, C., E. Y. Ersoy, H. Sözbilir, F. Erkül, O. Sümer, and B. Uzel (2009), Geochemistry and $^{40}Ar/^{39}Ar$ geochronology of Miocene volcanic rocks from the Karabarun Peninsula: Implications ofr amphibole-bearing lithospheric mantle source, Western Anatolia, *Journal of Volcanology and Geothermal Research*, *185*, 181–202, doi: j.jvolgeores.2009.05.016.

Herzberg, C., P. D. Asimow, N. Arndt, Y. Niu, C. M. Lesher, J. G. Fitton, M. J. Cheadle, and A. D. Saunders (2007), Temperatures in ambient mantle and plumes: constraints from basalts, picrites and komatiites, *Geochemistry, Geophysics, Geosystems*, *8*(2), doi: 10.1029/2006GC001390.

Hirschmann, M. M. (2010), Partial melt in the oceanic low velocity zone, *Physics of the Earth and Planetary Interiors*, *179*, 60–71, doi:10.1016/j.pepi.2009.12.003.

Hoggard, M. J., N. White, and D. Al-Attar (2016), Global dynamic topography observations reveal limited influence of large-scale mantle flow, *Nature Geoscience*, *9*, 456–463, doi:10.1038/ngeo2709.

Hoggard, M. J., J. Winterbourne, K. Czarnota, and N. White (2017), Oceanic residual depth measurements, the plate cooling model and global dynamic topography, *Journal of Geophysical Research: Solid Earth*, *122*(3), 2328–2372, doi:10.1002/2016JB013457.

Howard, A. D., and G. Kerby (1983), Channel changes in badlands, *Geological Society of America Bulletin*, *94*, 739–752.

Hubert-Ferrari, A., R. Armijo, G. King, B. Meyer, and B. Aykut (2002), Morphology, displacement, and slip-rates along the North Anatolian Fault, Turkey, *Journal of Geophysical Research*, *107*(B10), 2235, doi:10.1029/2001JB000393.

Hüsing, S. K., W.-J. Zachariasse, D. J. J. van Hinsbergen, W. Krijgsman, M. Inceoz, M. Harzhauser, O. Mandic, and A. Kroh (2009), Oligocene-Miocene basin evolution in SE Anatolia, Turkey: constraints on the closure of the eastern Tethys gateway, *Geological Society, London, Special Publications*, *311*(1), 107–132, doi:10.1144/SP311.4.

Innocenti, F., S. Agostini, G. Di Vincenzo, C. Doglioni, P. Manetti, M. Y. Savaşçin, and S. Tonarini (2005), Neogene and Quaternary volcanism in Western Anatolia: Magma sources and geodynamic evolution, *Marine Geology*, *221*(1-4), 397–421, doi: 10.1016/j.margeo.2005.03.016.

Isik, V., I. T. Uysal, A. Caglayan, and G. Seyitoglu (2014), The evolution of intraplate fault systems in central Turkey: Structural evidence and Ar-Ar and Rb-Sr age constraints for the Savcili Fault Zone, *Tectonics*, *33*(10), 1875–1899, doi: 10.1002/2014TC003565.

Jackson, J., and D. McKenzie (1988), The relationship between plate motions and seismic moment tensor, and the rates of active deformation in the Mediterranean and Middle East, *Geophysical Journal*, *93*, 45–73.

Jennings, E. S., and T. J. B. Holland (2015), A simple thermodynamic model for melting of peridotite in the system NCFMASOCr, *Journal of Petrology*, *56*(5), 869–892, doi: 10.1093/petrology/egv020.

Jolivet, L., and J. P. Brun (2010), Cenozoic geodynamic evolution of the Aegean, *International Journal of Earth Sciences*, *99*(1), 109–138, doi:10.1007/s00531-008-0366-4.

Karaoğlu, O., C. Helvacı, and Y. Ersoy (2010), Petrogenesis and $^{40}Ar/^{39}Ar$ geochronology of the volcanic rocks of the Uşak-Güre basin, western Türkiye, *Lithos*, *119*, 193–210, doi:10.1016/j.lithos.2010.07.001.

Karato, S.-i. (2011), Water distribution across the mantle transition zone and its implications for global material circulation, *Earth and Planetary Science Letters*, *301*, 413–423,

doi:10.1016/j.epsl.2010.11.038.

Katsura, T., H. Yamada, O. Nishikawa, M. Song, A. Kubo, T. Shinmei, S. Yokoshi, Y. Aizawa, T. Yoshino, M. J. Walter, E. Ito, and K.-i. Funakoshi (2004), Olivine-wadsleyite transition in the system $(Mg,Fe)_2SiO_2$, *Journal of Geophysical Research: Solid Earth*, *109*(B02209), doi:10.1029/2003JB002438.

Katz, R. F., M. Spiegelmann, and C. H. Langmuir (2003), A new parameterization of hydrous mantle melting, *Geochemistry, Geophysics, Geosystems*, *4*(9), doi:10.1029/2002GC000433.

Kelley, K. A., T. Plank, S. Newman, E. M. Stolper, T. L. Grove, S. Parman, and E. H. Hauri (2010), Mantle melting as a function of water content beneath the Mariana Arc, *Journal of Petrology*, *51*(8), 1711–1738, doi:10.1093/petrology/egq036.

Kempton, P. D., J. G. Fitton, C. J. Hawkesworth, and D. S. Ormerod (1991), Isotopic and trace element constraints on the composition and evolution of the lithosphere beneath the southwestern United States, *Journal of Geophysical Research*, *96*(B8), 13,713–13,735, doi:10.1029/91JB00373.

Keskin, M. (2003), Magma generation by slab steepening and breakoff beneath a subduction-accretion complex: An alternative model for collision-related volcanism in Eastern Anatolia, Turkey, *Geophysical Research Letters*, *30*(24), 7–10, doi:10.1029/2003GL018019.

Keskin, M. (2007), Eastern Anatolia: A hotspot in a collision zone without a mantle plume, in *Plates, plumes and planetary processes*, edited by G. R. Foulger and D. M. Jurdy, pp. 693–722, The Geological Society of America, Boulder, Colorado, doi:10.1130/2007.2430(32), geological Society of America Special Paper 430.

Keskin, M., J. A. Pearce, and J. G. Mitchell (1998), Volcano-stratigraphy and geochemistry of collision-related volcanism on the Erzurum-Kars Plateua, northeastern Turkey, *Journal of Volcanology and Geothermal Research*, *85*, 355–404.

Kheirkhah, M., M. B. Allen, and M. Emami (2009), Quaternary syn-collision magmatism from the Iran/Turkey borderlands, *Journal of Volcanology and Geothermal Research*, *182*, 1–12, doi:10.1016/j.jvolgeores.2009.01.026.

Kind, R., T. Eken, F. Tilmann, F. Sodoudi, T. Taymaz, F. Bulut, X. Yuan, B. Can, and F. Schneider (2015), Thickness of the lithosphere beneath Turkey and surroundings from S-receiver functions, *Solid Earth*, *6*, 971–984, doi:10.5194/se-6-971-2015.

Klaver, M., T. Djuly, S. de Graaf, A. Sakes, J. Wijbrans, G. Davies, and P. Vroon (2015), Temporal and spatial variations in provenance of Eastern Mediterranean Sea: Implications for Aegean and Aeolian arc volcanism, *Geochemica et Cosmochimica Acta*, *153*, 149–168, doi:10.1016/j.gca.2015.01.007.

Klaver, M., G. R. Davies, and P. Z. Vroon (2016), Subslab mantle of African provenance infiltrating the Aegean mantle wedge, *Geology*, *44*(5), 367–370, doi:10.1130/G37627.1.

Kürkçüoğlu, B., M. Pickard, P. Şen, B. B. Hanan, K. Sayit, C. Plummer, E. Sen, T. Yurur, and T. Furman (2015), Geochemistry of mafic lavas from Sivas, Turkey and th eevolution of Anatolian lithosphere, *Lithos*, *232*, 229–241, doi:10.1016/j.lithos.2015.07.006.

Kürüm, S., A. Önal, D. Boztuğ, T. Spell, and M. Arslan (2008), $^{40}Ar/^{39}Ar$ age and geochemistry of the post-collisional Miocene Yamadağ volcanics in the Arapkir area (Malatya Province), eastern Anatolia, Turkey, *Journal of Asian Earth Science*, *33*, 229–251, doi:10.1016/j.jseaes.2007.12.001.

Langmuir, C. H., A. Bezoós, S. Escrig, and S. W. Parman (2006), Chemical Systematics and Hydrous Melting of the Mantle in Back-Arc Basins, in *Back-Arc Spreading Systems: Geological, Biological, Chemical, and Physical Interactions*, edited by D. M. Christie, C. R. Fisher, S.-M. Lee, and S. Givens, pp. 87–146, American Geophysical Union, doi:10.1029/166GM07, geophysical Monograpg Series 166.

Le Pichon, X., and C. Kreemer (2010), The Miocene-to-present kinematic evolution of the Eastern Mediterranean and Middle East and its implications for dynamics, *Annual Reviews of Earth and Planetary Sciences*, *38*, 323–351, doi:10.1146/annurev-earth-040809-152419.

Lebedev, V. A., S. N. Bubnov, O. Z. Dudauri, and G. T. Vashakidze (2008a), Geochronology of Pliocene volcanism in the Dzhavakheti Highland (the Lesser Caucasus). Part 1: Western part of the Dzhavakheti Highland, *Stratigraphy and Geological Correlation*, *16*(2), 204–224.

Lebedev, V. A., S. N. Bubnov, O. Z. Dudauri, and G. T. Vashakidze (2008b), Geochronology of Pliocene volcanism in the Dzhavakheti Highland (the Lesser Caucasus). Part 1: Eastern part of the Dzhavakheti Highland. Regional geological correlation, *Stratigraphy and Geological Correlation*, *16*(5), 553–574.

Lebedev, V. A., E. V. Sharkov, E. Ünal, and M. Keskin (2016a), Late Pleistocene Tendürek Volcano (Eastern Anatolia, Turkey): 2. Geochemistry and petrogenesis of the rocks, *Petrology*, *24*(2), 234–270, doi:10.1134/S0869591116020041.

Lebedev, V. A., E. V. Sharkov, E. Ünal, and M. Keskin (2016b), Late Pleistocene Tendürek Volcano (Eastern Anatolia, Turkey): 1. Geochronology and petrographic characteristics of igneous rocks, *Petrology*, *24*(2), 127–152, doi:10.1134/S0869591116020041.

Lee, C. T. A., P. Luffi, T. Plank, H. Dalton, and W. P. Leeman (2009), Constraints on the depths and temperatures of basaltic magma generation on Earth and other terrestrial planets using new thermobarometers for mafic magmas, *Earth and Planetary Science Letters*, *279*(1-2), 20–33, doi:10.1016/j.epsl.2008.12.020.

Lüdecke, T., T. Mikes, F. B. Rojay, M. A. Cosca, and A. Mulch (2013), Stable isotope-based reconstruction of Oligo-Miocene paleoenvironment and paleohydrology of Central Anatolian lake basins (Turkey), *Turkish Journal of Earth Sciences*, *22*(5), 793–819, doi:10.3906/yer-1207-11.

Lustrino, M., and M. Wilson (2007), The circum-Mediterranean anorogenic Cenozoic igneous province, *Earth-Science Reviews*, *81*, 1–65, doi:10.1016/j.earscirev.2006.09.002.

Lustrino, M., M. Keskin, M. Mattioli, V. A. Lebedev, A. Chugaev, E. Sharkov, and O. Kavak (2010), Early activity of the largest Cenozoic shield volcano in the circum-Mediterranean area: Mt. Karacadağ, SE Turkey, *European Journal of Mineralogy*, *22*, 343–362, doi:10.1127/0935-1221/2010/0022-2024.

Lustrino, M., M. Keskin, M. Mattioli, and O. Kavak (2012), Heterogenous mantle sources feeding the volcanic activity of Mt. Karacadağ (SE Turkey), *Journal of Asian Earth Sciences*, *46*, 120–139, doi:10.1016/j.jseaes.2011.11.016.

Matthews, S., O. Shorttle, and J. Maclennan (2016), The temperature of the Icelandic mantle from olivine-spinel aluminum exchange thermometry, *Geochemistry, Geophysics, Geosystems*, *17*, 4725–4752, doi:10.1002/2016GC006497.

McKenzie, D. (1978), Active tectonics of the Alpine-Himalayan belt: the Aegean Sea and surrounding regions, *Geophysical Journal of the Royal Astronomical Society*, *55*, 217–254.

McKenzie, D. (2003), Estimating T_e in the presence of internal loads, *Journal of Geophysical Research*, *108*(B9), 2438, doi:10.1029/2002JB001766.

McKenzie, D. (2010), The influence of dynamically supported topography on estimates of T_e, *Earth and Planetary Science Letters*, *295*(1–2), 127–138, doi:10.1016/j.epsl.2010.03.033.

McKenzie, D., and M. J. Bickle (1988), The volume and composition of melt generated by extension of the lithosphere, *Journal of Petrology*, *29*(3), 625–679.

McKenzie, D., and D. Fairhead (1997), Estimates of the effective elastic thickness of the continental lithosphere from Bouger and free air gravity anomalies, *Journal of Geophysical Research*, *102*(B12), 27,523–27,552, doi:10.1007/s13137-015-0078-4.

McKenzie, D., and R. K. O'Nions (1991), Partial melt distributions from inversion of rare earth element concentrations, *Journal of Petrology*, *32*(5), 1021–1091.

McQuarrie, N., and D. J. J. Van Hinsbergen (2013), Retrodeforming the Arabia-Eurasia collision zone: Age of collision versus magnitude of continental subduction, *Geology*, *41*(3), 315–318, doi:10.1130/G33591.1.

1562 Michael, P. (1995), Regionally distinctive sources of depleted MORB: Evidence from
1563 trace elements and H_2O, *Earth and Planetary Science Letters*, *131*(3–4), 301–320, doi:
1564 10.1016/0012-821X(95)00023-6.
1565 Molinari, I., and A. Morelli (2011), EPcurst: a reference model for the European
1566 Plate, *Geophysical Journal International*, *185*(1), 352–364, doi:10.1111/j.1365-
1567 246X.2011.04940.x.
1568 Neill, I., K. Meliksetian, M. B. Allen, G. Navasardyan, and K. Kuiper (2015), Petrogen-
1569 esis of mafic collision zone magmatism: The Armenian sector of the Turkish-Iranian
1570 Plateau, *Chemical Geology*, *403*, 24–41, doi:10.1016/j.chemgeo.2015.03.013.
1571 Nocquet, J.-M. (2012), Present-day kinematics of the Mediterranean: A com-
1572 prehensive overview of GPS results, *Tectonophysics*, *579*, 220–242, doi:
1573 10.1016/j.tecto.2012.03.037.
1574 Olsen, P., G. Schubert, C. Anderson, and P. Goldman (1988), Plume formation and litho-
1575 sphere erosion: a comparison of laboratory and numerical experiments, journal = Jour-
1576 nal of Geophysical Research, volume = 93, number = B12, pages = 15,065–15,084.
1577 Oyan, V., M. Keskin, V. A. Lebedev, A. V. Chugaev, and E. V. Sharkov (2016), Magmatic
1578 evolution of the Early Pliocene Etrüsk stratovolcano, Eastern Anatolia Collision Zone,
1579 Turkey, *Lithos*, *256–257*, 88–108, doi:10.1016/j.lithos.2016.03.017.
1580 Özdemir, Y., and N. Güleç (2013), Geological and geochemical evolution of the quater-
1581 nary Süphan Stratovolcano, Eastern Anatolia, Turkey: Evidence for the lithosphere-
1582 asthenosphere interaction in post-collisional volcanism, *Journal of Petrology*, *55*(1), 37–
1583 62, doi:doi:10.1093/petrology/egt060.
1584 Özdemir, Y., O. Karaoğlu, A. U. Tolluoğlu, and N. Güleç (2006), Volcanostratigraphy and
1585 petrogenesis of the Nemrut stratovolcano (East Anatolian High Plateau): The most
1586 recent post-collisional volcanism in Turkey, *Chemical Geology*, *226*, 189–211, doi:
1587 10.1016/j.chemgeo.2005.09.020.
1588 Parlak, O., A. Kop, U. C. Ünlügenç, and C. Demirkol (1998), Geochronology and geo-
1589 chemistry of basaltic rocks in the Karasu Graben around Kırıkhan (Hatay), S. Turkey,
1590 *Turkish Journal of Earth Sciences*, *7*, 53–61.
1591 Parlak, O., M. Delaloye, C. Demirkol, and U. C. Ünlügenç (2001), Geochemistry of
1592 Pliocene/Pleistocene basalts along the Central Anatolian Fault Zone (CAFZ), Turkey,
1593 *Geodinamic Acta*, *14*, 159–167.
1594 Paton, S. M. (1992), The relationship between extension and volcanism in Western
1595 Turkey, the Aegean Sea and Central Greece, Ph.D. thesis, University of Cambridge.
1596 Paul, J. D., G. G. Roberts, and N. White (2014), The African landscape through space and
1597 time, *Tectonics*, *33*(6), 898–935, doi:10.1002/2013TC003479.
1598 Pearce, J., J. Bender, S. De Long, W. Kidd, P. Low, Y. Güner, F. Saroglu, Y. Yilmaz,
1599 S. Moorbath, and J. Mitchell (1990), Genesis of collision volcanism in Eastern Ana-
1600 tolia, Turkey, *Journal of Volcanology and Geothermal Research*, *44*, 189–229, doi:
1601 10.1016/0377-0237(90)90018-B.
1602 Philpotts, A. R., and J. J. Ague (2009), *Principles of Igneous and Metamorphic Petrology*,
1603 2 ed., Cambridge University Press, Cambridge, U.K., doi:10.1017/CBO9780511813429.
1604 Plank, T., and D. Forsyth (2016), Thermal structure and melting conditions in the mantle
1605 beneath the Basin and Range province from seismology and petrology, *Geochemistry,*
1606 *Geophysics, Geosystems*, *17*, 1312–1338, doi:10.1002/2015GC006205.
1607 Plank, T., and C. H. Langmuir (1998), The chemical composition of subducting sediment
1608 and its consequences for the crust and mantle, *Chemical Geology*, *145*, 325–394, doi:
1609 10.1016/S0009-2541(97)00150-2.
1610 Poisson, A., J. C. Guezou, A. Ozturk, S. Inan, H. Temiz, H. Gürsöy, K. S. Kavak,
1611 and S. Özden (1996), Tectonic setting and evolution of the Sivas Basin, cen-
1612 tral Anatolia, Turkey, *International Geology Review*, *38*(9), 838–853, doi:
1613 10.1080/00206819709465366.
1614 Poisson, A., F. Orszag-Sperber, E. Kosun, M.-A. Bassetti, C. Müller, R. Wernlu, and J.-
1615 M. Rouchy (2011), The late Cenozoic evolution of the Aksu basin (Isparta Angle; SW

Turkey). New Insights, *Bulletin de la Société Géologique de France*, *182*(2), 133–148.

Polat, A., R. Kerrich, and J. F. Casey (1997), Geochemistry of Quaternary basalts erupted along the East Anatolian and Dead Sea fault zones of southern Turkey: implications for mantle sources, *Lithos*, *40*, 55–68.

Prelević, D., C. Akal, S. F. Foley, R. L. Romer, A. Stracke, and P. van den Bogaard (2012), Ultrapotassic mafic rocks as geochemical proxies for post-collisional dynamics of orogenic lithospheric mantle: the case of southwestern Anatolia, Turkey, *Journal of Petrology*, *53*(5), 1019–1005, doi:10.1093/jpetrology/egs008.

Prelević, D., C. Akal, R. L. Romer, R. Mertz-Kraus, and C. Helvacı (2015), Magmatic response to slab tearing: Constraints from the Afyon Alkaline Volcanic Complex, Western Turkey, *Journal of Petrology*, *56*(3), 527–562, doi:10.1093/petrology/egv008.

Press, W. H., S. A. Teukolsky, W. T. Vetterling, and B. P. Flannery (1992), *Numerical recipes in Fortran: the art of scientific computing*, Cambridge University Press, Cambridge, UK.

Priestley, K., and D. McKenzie (2013), The relationship between shear wave velocity, temperature, attenuation and viscosity in the shallow part of the mantle, *Earth and Planetary Science Letters*, *381*, 78–91, doi:10.1016/j.epsl.2013.08.022.

Pritchard, D., G. G. Roberts, N. J. White, and C. N. Richardson (2009), Uplift histories from river profiles, *Geophysical Research Letters*, *36*(24), 1–5, doi:10.1029/2009GL040928.

Putirka, K. D., M. Perfit, F. J. Ryerson, and M. G. Jackson (2007), Ambient and excess mantle temperatures, olivine thermometry, and active vs. passive upwelling, *Chemical Geology*, *241*, 177–206, doi:10.1016/j.chemgeo.2007.01.014.

Reid, M. R., W. K. Schleiffarth, M. A. Cosca, J. R. Delph, J. Blichert-Toft, and K. M. Cooper (2017), Shallow melting of MORB-like mantle under hot continental lithosphere, Central Anatolia, *Geochemistry, Geophysics, Geosystems*, *18*, 1866–1888, doi:10.1002/2016GC006772.

Reilinger, R., S. McClusky, P. Vernant, S. Lawrence, S. Ergintav, R. Cakmak, H. Ozener, F. Kadirov, I. Guliev, R. Stepanyan, M. Nadariya, G. Hahubia, S. Mahmoud, K. Sakr, A. ArRajehi, D. Paradissis, A. Al-Aydrus, M. Prilepin, T. Guseva, E. Evren, A. Dmitrotsa, S. V. Filikov, F. Gomez, R. Al-Ghazzi, and G. Karam (2006), GPS constraints on continental deformation in the Africa-Arabia-Eurasia continental collision zone and implications for the dynamics of plate interactions, *Journal of Geophysical Research: Solid Earth*, *111*(5), 1–26, doi:10.1029/2005JB004051.

Richards, F. D., M. J. Hoggard, and N. J. White (2016), Cenozoic epeirogeny of the Indian peninsula, *Geochemistry, Geophysics, Geosystems*, *17*, 4920–4954, doi:10.1002/2016GC006545.

Richardson-Bunbury, J. M. (1992), Basalts of Kula and their relation to extension in western Turkey, Ph.D. thesis, University of Cambridge.

Roberts, G. G., and N. White (2010), Estimating uplift rate histories from river profiles using African examples, *Journal of Geophysical Research: Solid Earth*, *115*(2), 1–24, doi:10.1029/2009JB006692.

Rudge, J. F., G. G. Roberts, N. J. White, and C. N. Richardson (2015), Uplift histories of Africa and Australia from linear inverse modeling of drainage inventories, *Journal of Geophysical Research F: Earth Surface*, *120*(5), 894–914, doi:10.1002/2014JF003297.

Salaün, G., H. A. Pedersen, A. Paul, V. Farra, H. Karabulut, D. Hatzfeld, C. Papazachos, D. M. Childs, and C. Pequegnat (2012), High-resolution surface wave tomography beneath the Aegean-Anatolia region: Constraints on upper-mantle structure, *Geophysical Journal International*, *190*(1), 406–420, doi:10.1111/j.1365-246X.2012.05483.x.

Saunders, P., K. Priestley, and T. Taymaz (1998), Variations in the crustal structure beneath western Turkey, *Geophysical Journal International*, *134*, 373–389.

Schemmel, F., T. Mikes, B. Rojay, and A. Mulch (2013), The impact of topography on isotopes in precipitation across the Central Anatolian Plateau (Turkey), *American Journal of Science*, *313*, 61–80, doi:10.2475/02.2013.01.

Schildgen, T. F., D. Cosentino, B. Bookhagen, S. Niedermann, C. Yıldırım, H. Echtler, H. Wittmann, and M. R. Strecker (2012a), Multi-phased uplift of the southern margin of the Central Anatolian plateau, Turkey: A record of tectonic and upper mantle processes, *Earth and Planetary Science Letters*, *317-318*, 85–95, doi:10.1016/j.epsl.2011.12.003.

Schildgen, T. F., D. Cosentino, A. Caruso, R. Buchwaldt, C. Yıldırım, S. A. Bowring, B. Rojay, H. Echtler, and M. R. Strecker (2012b), Surface expression of eastern Mediterranean slab dynamics: Neogene topographic and structural evolution of the southwest margin of the Central Anatolian Plateau, Turkey, *Tectonics*, *31*(2), doi: 10.1029/2011TC003021.

Schildgen, T. F., C. Yıldırım, D. Cosentino, and M. R. Strecker (2014), Linking slab break-off, Hellenic trench retreat, and uplift of the Central and Eastern Anatolian plateaus, *Earth-Science Reviews*, *128*, 147–168, doi:10.1016/j.earscirev.2013.11.006.

Semiz, B., E. Y. Ersoy, Y. Özpınar, C. Helvacı, M. R. Palmer, and M. Z. Billor (2015), ^{40}Ar/^{39}Ar geochronology, geochemistry and petrology of volcanic rocks from the Simav Graben, western Turkey, *Contributions to Mineral Petrology*, *170*, 24, doi: 10.1007/s00410-015-1178-8.

Şengör, A. M. C., and Y. Yilmaz (1981), Tethyan evolution of Turkey: A plate tectonic approach, *Tectonophysics*, *75*(3-4), doi:10.1016/0040-1951(81)90275-4.

Şengör, A. M. C., N. Görür, and Şaroğlu (1985), Strike-slip faulting and related basin formation in zones of tectonic escape: Turkey as a case study, in *Strike-slip deformation, baisn formation, and sedimentation*, vol. 37, edited by K. T. Biddle and N. Christie-Black, pp. 227–264, Society for Economical Paleontology and Mineralogy Special Publication, Tulsa, USA, doi:10.2110/pec.85.37.0227.

Şengör, A. M. C., S. Özeren, T. Genç, and E. Zor (2003), East Anatolian high plateau as a mantle-supported, north-south shortened domal structure, *Geophysical Research Letters*, *30*(24), 2–5, doi:10.1029/2003GL017858.

Şengör, A. M. C., M. S. Özeren, M. Keskin, M. Sakinç, A. D. Özbakir, and I. Kayan (2008), Eastern Turkish high plateau as a small Turkic-type orogen: Implications for post-collisional crust-forming processes in Turkic-type orogens, *Earth-Science Reviews*, *90*(1-2), 1–48, doi:10.1016/j.earscirev.2008.05.002.

Seyitoğlu, G., D. Anderson, G. Nowell, and B. Scott (1997), The evolution from Miocene potassic to Quaternary sodic magmatism in western Turkey: implications for enrichment processes in the lithospheric mantle, *Journal of Volcanology and Geothermal Research*, *76*, 127–147.

Sklar, L., and W. E. Dietrich (1998), River longitudinal profiles and bedrock incision models: Stream power and the influence of sediment supply, in *Rivers over rock: fluvial processes in bedrock channels*, *Geophysical Monograph Series*, vol. 107, edited by K. J. Tinkler and E. E. Wohl, pp. 237–260, American Geophysical Union, San Francisco, USA.

Skolbeltsyn, G., R. Mellors, R. Gök, N. Türkelli, G. Yetirmishli, and E. Sandvol (2014), Upper mantle S wave velocity structure of the East Anatolian-Caucasus region, *Tectonics*, *33*(3), 207–221, doi:10.1002/2013TC003334.

Stracke, A., A. W. Hofmann, and S. R. Hart (2005), FOZO, HIMU, and the rest of the mantle zoo, *Geochemistry, Geophysics, Geosystems*, *6*(5), doi:10.1029/2004GC000824.

Taghizadeh-Farahmand, F., F. Sodoudi, N. Afsari, and M. R. Ghassemi (2010), Lithospheric structure of NW Iran from *P* and *S* receiver functions, *Journal of Seismology*, *14*, 823–836, doi:10.1007/s10950-010-9199-2.

Tapley, B. D., J. Ries, S. Bettadpur, D. Chambers, M. Cheng, F. Condi, and S. Poole (2007), The GGM03C Mean Earth Gravity Model from GRACE, in *Eos Transactions*, vol. 88, abstract G42A-03 presented at AGU Fall Meeting 2017, San Francisco, USA.

Tarboton, D. G. (1997), A new method for the determination of flow directions and upslope areas in grid elevation models, *Water Resources Research*, *33*(2), 309–319, doi: 10.1029/96WR03137.

Temel, A., T. Yüruür, P. Alıcı, E. Varol, A. Gourgaud, H. Bellon, and H. Demirbağ (2010), Alkaline series related to Early-Middle Miocene intra-continental rifting in a collision zone: An example from Polatlı, Central Anatolia, Turkey, *Journal of Asain Earth Science*, *38*, 298–306, doi:10.1016/j.jseaes.2009.12.017.

Tezel, T., T. Shibutani, and B. Kaypak (2010), Crustal variation in western Turkey inferred from the receiver function analysis, *Tectonophysics*, *492*, 240–252, doi: 10.1016/j.tecto.2010.06.006.

Tezel, T., T. Shibutani, and B. Kaypak (2013), Crustal thickness of turkey determined by receiver function, *Journal of Asian Earth Sciences*, *75*, 36–45, doi: 10.1016/j.jseaes.2013.06.016.

Thompson, R. N., C. J. Ottley, P. M. Smith, D. Pearson, G., A. P. Pickin, M. A. Morrison, P. T. Leat, and S. A. Gibson (2005), Source of Quaternary alkalic basalts, picrites and basanites of the Potrillo Volcanic Field, New Mexico, USA: lithosphere or convecting mantle?, *Journal of Petrology*, *46*(8), 1603–1643, doi:10.1093/petrology/egi028.

Tomkin, J. H., M. T. Brandon, F. J. Pazzaglia, J. R. Barbour, and S. D. Willett (2003), Quantitative testing of bedrock incision models for Clearwater River, NW Washington State, *Journal of Geophysical Research*, *108*(B8), 2308, doi:10.1029/2001JB000862.

Tunoğlu, C. (1991), Orta Pontidler'de Devrekani Havzası'nın (Kastamonu kuzeyi) lithostratigrafi birimleri, in *Suat Erk Jeoloji Sempozyumu, Bildiriler Kitabı*, pp. 183–191, Ankara Üniversitesi, Fen Fakültesi, Ankara.

Tunoğlu, C. (1994), Microfacies analysis of the upper Paleocene–middle Eocene carbonate sequence Devrekani Basin (Northern Kastamonu), *Geological Bulletin of Turkey*, *37*(2), 43–51.

Uluocak, E. Ş., R. Pysklywec, and O. H. Göğüş (2016), Present-day dynamic and residual topography in Central Anatolia, *Geophysical Journal International*, *206*(3), 1515–1525, doi:10.1093/gji/ggw225.

van der Meijde, M., S. van der Lee, and D. Giardini (2003), Crustal structure beneath broad-band seismic stations in the Mediterranean region, *Geophysical Journal International*, *152*, 729–739.

van Hinsbergen, D. J. J., N. Kaymakci, W. Spakman, and T. H. Torsvik (2010), Reconciling the geological history of western Turkey with plate circuits and mantle tomography, *Earth and Planetary Science Letters*, *297*(3-4), 674–686, doi:10.1016/j.epsl.2010.07.024.

van Hunen, J., and M. B. Allen (2011), Continental collision and slab break-off: A comparison of 3-D numerical models with observations, *Earth and Planetary Science Letters*, *302*, 27–37, doi:10.1016/j.epsl.2010.11.035.

Vanacore, E. A., T. Taymaz, and E. Saygin (2013), Moho structure of the Anatolian Plate from receiver function analysis, *Geophysical Journal International*, *193*, 329–337, doi: 10.1093/gji/ggs107.

Varol, E., A. Temel, T. Yürür, A. Gourgaud, and H. Bellon (2014), Petrogenesis of the Neogene bimodal magmatism of the Galatean Volcanic Province, Central Anatolia, Turkey, *Journal of Volcanology and Geothermal Research*, *280*, 14–29, doi: 10.1016/j.jvolgeores.2014.04.014.

Walsh-Kennedy, S., A. Aksu, J. Hall, R. Hiscott, C. Yaltırak, and C. Çifçi (2014), Source ot sink: The development of the latest Messinian to Pliocene-Quaternary Cilicia and Adana Basins and their linkages with the onland Mut Basin, eastern Mediterranean, *Tectonophysics*, *622*, 1–21, doi:10.1016/j.tecto.2014.01.019.

Whipple, K. X. (2009), The influence of climate on the tectonic evolution of mountain belts, *Nature Geoscience*, *2*, 97–104, doi:10.1038/NGEO413.

Whipple, K. X., and G. E. Tucker (1999), Dynamics of the stream-power river incision model: implications for height limits of mountain ranges, landscape response times, and research needs, *Journal of Geophysical Research*, *104*(B8), 17,661–17,644, doi: 10.1029/1999JB900120.

Whipple, K. X., and G. E. Tucker (2002), Implications of sediment-flux dependent river incision models for landscape evolution, *Journal of Geophysical Research*, *107*(B2), doi:

10.1029/2000JB000044.

Willett, S. D., S. W. McCoy, J. T. Perron, and C.-Y. Chen (2014), Dynamic reorganization of river basins, *Science*, *343*, 1248,765, doi:10.1126/science.124875.

Wilson, J. W. P., G. G. Roberts, M. J. Hoggard, and N. J. White (2014), Cenozoic epeirogeny of the Arabian Peninsula from drainage modeling, *Geochemistry, Geophysics, Geosystems*, *15*, 3723–3761, doi:10.1002/2014GC005283.

Wilson, M., A. Tankut, and N. Guleç (1997), Tertiary volcanism of the Galatia province, north-west Central Anatolia, Turkey, *Lithos*, *42*(1–2), 105–121, doi:10.1016/S0024-4937(97)00039-X.

Yamauchi, H., and Y. Takei (2016), Polycrystal anelasticity at near-solidus temperatures, *Journal of Geophysical Research: Solid Earth*, *121*, 7790–7820, doi:10.1002/2016JB013316.

Yıldırım, C., T. F. Schildgen, H. Echtler, D. Melnick, and M. R. Strecker (2011), Late Neogene and active orogenic uplift in the Central Pontides associated with the North Anatolian Fault: Implications for the northern margin of the Central Anatolian Plateau, Turkey, *Tectonics*, *30*(TC5005), doi:10.1029/2010TC002756.

Yıldırım, C., D. Melnick, P. Ballato, T. F. Schildgen, H. Echtler, A. E. Erginal, N. G. Kıyak, and M. F. Strecker (2013), Differential uplift along the northern margin of the Central Anatolian Plateau: inferences from marine terraces, *Quaternary Science Reviews*, *81*, 12–28, doi:10.1016/j.quascirev.2013.09.011.

Yıldırım, C., M. A. Sarikaya, and A. Çiner (2016), Late Pleistocene intraplate extension of the Central Anatolian Plateau, Turkey: Inferences from cosmogenic exposure dating of alluvial fan, landslide, and moraine surfaces along the Ecemiş Fault Zone, *Tectonics*, *35*(6), 1446–1464, doi:10.1002/2015TC004038.

Yıldız, A., V. Toker, H. Demircan, and S. Sevim (2003), Paleoenvironmental interpretation and findings of Pliocene-Pleistocene nannoplankton, planktic foraminifera, trace fossil in the Mut Basin, *Yerbilimleri*, *28*, 123–144.

Zhu, L., B. J. Mitchell, N. Akyol, I. Cemen, and K. Kekovali (2006), Crustal thickness variations in the Aegean region and implications for the extension of continental crust, *Journal of Geophysical Research*, *111*.

Zindler, A., and S. Hart (1986), Chemical Geodynamics, *Annual Reviews of Earth and Planetary Sciences*, *14*, 493–571.

Zor, E., E. Sandvol, C. Gürbüz, N. Türkelli, D. Seber, and M. Barazangi (2003), The crustal structure of the East Anatolian plateau (Turkey) from receiver functions, *Geophysical Research Letters*, *30*(24), 8044, doi:10.1029/2003GL018192.

Zor, E., S. Özalaybey, and C. Gürbüz (2006), The crustal structure of the eastern Marmara region, Turkey by teleseismic receiver functions, *Geophysical Journal International*, *167*, 213–222, doi:10.1111/j.1365-246X.2006.03042.x.